Scaling of an existing 60 kN LOX/LCH$_4$ combustion down to a liquid 2.5 kN HTP/Kerosene combustion of an innovative hyperboloid rocket engine in Ansys Fluent

Masterarbeit von
Bruno Josef Müller

IRS-25-S-074

Hochschullehrer/in:
apl. Prof. Dr.-Ing. Georg Herdrich

Betreuer/in:
Black Engine Aerospace: Dr. Artur Schimpf
DLR Stuttgart: Markus Ortelt
DLR Stuttgart: Dr. Peter Ess
DLR Köln: Thorn Schleutker

Deutsches Zentrum für Luft- und Raumfahrt, Stuttgart
Black Engine Aerospace GmbH, Heilbronn
Institut für Raumfahrtsysteme
Universität Stuttgart

September 2025

UNIVERSITÄT STUTTGART
INSTITUT FÜR RAUMFAHRTSYSTEME
im Raumfahrtzentrum Baden-Württemberg (RZBW)

Pfaffenwaldring 29 · 70569 Stuttgart · Tel.: (0711) 685-62375 · www.irs.uni-stuttgart.de

Aufgabenstellung Masterarbeit

für Herrn Bruno Müller

Größen- und Leistungsskalierung einer existierenden Sauerstoff-Methan-Verbrennung einer innovativen 60 kN-Hyperboloid-Flüssigraketenbrennkammer hin zur Wasserstoffperoxid-Kerosin-Verbrennung der 2,5 kN Schubklasse in Ansys-Fluent.

Scaling of an existing 60 kN LOX/LCH4 combustion down to a liquid 2.5 kN HTP/Kerosene combustion of an innovative hyperboloid rocket engine in Ansys-Fluent

Motivation:

Das am DLR im Rahmen der keramischen transpirationsgekühlten Raketenschubammer-Technologie entwickelte Dualschalen-Hyperboloid-Brennkammerdesign verspricht durch das sog. ‚Injection-Cooling' zahlreiche Vorteile gegenüber dem klassischen Zylinder-Laval-Design flüssiger Hochleistungs-Raumfahrtantriebe. In Ansys-Fluent wurde dbzgl. bereits die LOX-LCH4-Verbrennung in einer Brennkammer der 6-Tonnen-Schubklasse für Stufentriebwerke von Mini-Launchern verifizierend untersucht. Darüber hinaus soll nun die besonders herausfordernde Verbrennung von HTP und Jet-A1 derart numerisch untersucht werden, dass das durch die poröse keramische Brennkammerwand in den Brennraum hineindiffundierende Jet-A1 (s. Abbildung oben PC2) mit vorstabilisiertem und im Injektor zu H2O und O2 dekomponiertem HTP 95% (PC1) reagiert. Ziel ist dabei eine Schubklasse von 2,5 kN in einem realitätsnahen Schubkammerdesign, welches bei einem asiatischen Entwicklungspartner zur Vermarktung vorgesehen ist. Die Arbeit wird am DLR-Institut für Bauweisen und Strukturtechnologie in Stuttgart durchgeführt und extern von der Black Engine Aerospace GmbH (BEA) mitbetreut.

Aufgabenstellung:

- Einarbeitung in die Thematik der Flüssigraketenantriebe
- Festlegung von Modellrandbedingungen u.a. auf Basis vorhandener Testergebnisse bei GOX/GH2-Verbrennung gegen Kerosin-Diffusion durch die poröse Keramikwand.
- Skalierung des 60-kN-LOX/LCH4-Fluent-Modells auf das 2,5 kN HTP/Jet-A1-Triebwerk
- Dokumentation und Präsentation

Die Arbeit wird am DLR Stuttgart durchgeführt.

Betreuer/-in intern: apl. Prof. Dr. G. Herdrich (IRS)

Betreuer/-in extern: Markus Ortelt, Dr. Peter Ess (DLR), Dr. Artur Schimpf (BEA)

Bearbeitungsbeginn: 07.03.2025

Einzureichen spätestens: 07.09.2025

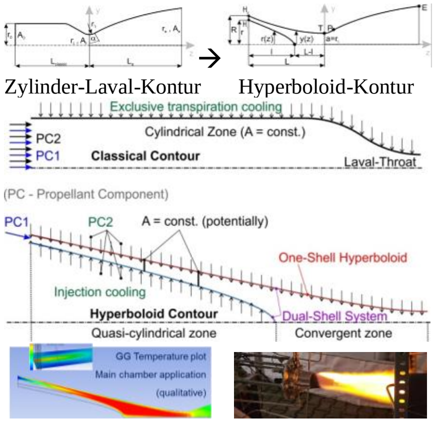

Empfangsbestätigung:
Ich bestätige hiermit, dass ich die Aufgabenstellung sowie die rechtlichen Bestimmungen und die Studien- und Prüfungsordnung gelesen und verstanden habe.

07.09.2025 gez. Herdrich
Datum
apl. Prof. Dr.-Ing. Georg Herdrich
(Verantwortlicher Hochschullehrer)

07.09.2025 gez. Ortelt
Datum
Externe/r Betreuer/-in

07.09.2025 gez. Bruno Müller
Datum
Unterschrift des/der Studierenden

Rechtliche Bestimmungen: Der/die Bearbeiter/in ist grundsätzlich nicht berechtigt, irgendwelche Arbeits- und Forschungsergebnisse, von denen er/sie bei der Bearbeitung Kenntnis erhält, ohne Genehmigung des/der Betreuers/in dritten Personen zugänglich zu machen. Bezüglich erreichter Forschungsleistungen gilt das Gesetz über Urheberrecht und verwendete Schutzrechte (Bundesgesetzblatt I/ S. 1273, Urheberschutzgesetz vom 09.09.1965). Der/die Bearbeiter/in hat das Recht, seine/ihre Erkenntnisse zu veröffentlichen, soweit keine Erkenntnisse und Leistungen der betreuenden Institute und Unternehmen eingeflossen sind. Die von der Studienrichtung erlassenen Richtlinien zur Anfertigung der Masterarbeit sowie die Prüfungsordnung sind zu beachten.

Erklärungen

Hiermit versichere ich, **Müller**, **Bruno,** dass ich diese ***Masterarbeit*** selbstständig mit Unterstützung des Betreuers / der Betreuer angefertigt und keine anderen als die angegebenen Quellen und Hilfsmittel verwendet habe. Die Arbeit oder wesentliche Bestandteile davon sind weder an dieser noch an einer anderen Bildungseinrichtung bereits zur Erlangung eines Abschlusses eingereicht worden.

Ich erkläre weiterhin, bei der Erstellung der Arbeit die einschlägigen Bestimmungen zum Urheberschutz fremder Beiträge entsprechend den Regeln guter wissenschaftlicher Praxis[1] eingehalten zu haben. Soweit meine Arbeit fremde Beiträge (z.B. Bilder, Zeichnungen, Textpassagen etc.) enthält, habe ich diese Beiträge als solche gekennzeichnet (Zitat, Quellenangabe) und eventuell erforderlich gewordene Zustimmungen der Urheber zur Nutzung dieser Beiträge in meiner Arbeit eingeholt. Mir ist bekannt, dass ich im Falle einer schuldhaften Verletzung dieser Pflichten die daraus entstehenden Konsequenzen zu tragen habe.

Des Weiteren erkläre ich, dass die von mir elektronisch eingereichte Ausführung dieser Abschlussarbeit mit den gebundenen Exemplaren übereinstimmt.

Stuttgart, 07.09.2025, gez. Bruno Müller

Ort, Datum, Unterschrift

Hiermit erkläre ich mich damit einverstanden, dass meine ***Masterarbeit*** zum Thema:

Scaling of an existing 60 kN LOX/LCH4 combustion down to a liquid 2.5 kN HTP/Kerosene combustion of an innovative hyperboloid rocket engine in Ansys Fluent

in der Institutsbibliothek des Instituts für Raumfahrtsysteme ohne Sperrfrist öffentlich zugänglich aufbewahrt und die Arbeit auf der Institutswebseite sowie im Online-Katalog der Universitätsbibliothek erfasst wird. Letzteres bedeutet eine dauerhafte, weltweite Sichtbarkeit der bibliographischen Daten der Arbeit (Titel, Autor, Erscheinungsjahr, etc.).

Nach Abschluss der Arbeit werde ich zu diesem Zweck meinem Betreuer neben dem Prüfexemplar eine weitere gedruckte sowie eine digitale Fassung übergeben.

Der Universität Stuttgart übertrage ich das Eigentum an diesen zusätzlichen Fassungen und räume dem Institut für Raumfahrtsysteme an dieser Arbeit und an den im Rahmen dieser Arbeit von mir erzeugten Arbeitsergebnissen ein kostenloses, zeitlich und örtlich unbeschränktes, einfaches Nutzungsrecht für Zwecke der Forschung und der Lehre ein. Falls in Zusammenhang mit der Arbeit Nutzungsrechtsvereinbarungen des Instituts mit Dritten bestehen, gelten diese Vereinbarungen auch für die im Rahmen dieser Arbeit entstandenen Arbeitsergebnisse.

Stuttgart, 07.09.2025, gez. Bruno Müller

Ort, Datum, Unterschrift

---

[1] Nachzulesen in den DFG-Empfehlungen zur „Sicherung guter wissenschaftlicher Praxis“ bzw. in der Satzung der Universität Stuttgart zur „Sicherung der Integrität wissenschaftlicher Praxis und zum Umgang mit Fehlverhalten in der Wissenschaft“

Abstract

In this thesis, the combustion of an innovative 60 kN LOX/CH_4 Dual Shell Hyperboloid Rocket Engine is being scaled down to a 2.5 kN HTP/kerosene Dual Shell Hyperboloid Rocket Engine. Dual-shell hyperboloid engines use a new approach to the design of the combustion chamber and cooling in rocket engines, which can prove advantageous over conventional rocket engines. The scaling takes place as a part of the DeRisk project at the Black Engine Aerospace company which is a DLR-spin-off. A CFD analysis of the new engine is performed in Ansys Fluent. The goal is to obtain a meaningful initial estimate of the flow field, combsution, and performance parameters of the engine and to then compare it with the results from previous tests from other engines of the DeRisk project. For this purpose, a comprehensive flow model is designed and implemented. Using a single-stage combustion model according to Zeng et al. (2014), the 3D model of the engine is examined, and a mesh study ensures the validity of the results. The results show that the engine generates a thrust of 2.2 kN, thus falling just short of the target performance of 2.5 kN. A detailed analysis of the flow field reveals insufficient mixing of the fuel components in the combustion chamber, which leads to combustion losses. This is inconsistent with tests from previous engines in the DeRisk project–there the parameters point to a more sufficient combustion completeness. This raises questions about whether the CFD model is capable of accurately representing the real conditions of the new engine and whether the new engine exhibits combustion characteristics in tests that are as good as its predecessors. For this reason, it is recommended that the CFD model be further refined in future work and that tests be carried out on the new engine in order to validate the results of the present and future simulations.

Kurzfassung

In der vorliegenden Arbeit wird die Verbrennung eines innovativen 60-kN-LOX/CH_4-Dualschalen-Hyperboloid-Raketentriebwerks auf ein 2,5-kN-HTP/Kerosin-Dualschalen-Hyperboloid-Raketentriebwerk herunterskaliert. Dualschalen-Hyperboltriebwerke verfolgen einen neuen Ansatz zur Gestaltung der Brennkammer und der Kühlung in Raketentriebwerken welche sich gegenüber herkömmlichen Raketentriebwerken vorteilhaft erweisen können. Die Skalierung findet im Rahmen des DeRisk Projekts der Firma Black Engine Aerospace, welche ein aus dem DLR ausgegründetes Start-up-Unternehmen ist und sich als Ziel gesetzt hat, Dualschalen-Hyperboloidtriebwerke zur Serienreife zu entwickeln. Die Skalierung besteht daraus, das neue Triebwerk in Ansys Fluent als CFD-Simulation zu modellieren und die Ergebnisse mit den mit den Ergebnissen aus den Tests vorheriger Triebwerke aus dem DeRisk Projekt zu vergleichen. Hierzu wird ein umfangreiches Strömungsmodell entworfen und umgesetzt mit dem Ziel eine aussagekräftige erste Abschätzung des Strömungsfelds, der Verbrennung und Leistungsparameter des Triebwerks zu erhalten. Unter Verwendung eines einstufigen Verbrennungsmodells nach Zeng et al. (2014) wird das 3D-Modell des Triebwerks untersucht und eine Netzstudie stellt die Validität der Ergebnisse sicher. Die Ergebnisse zeigen, dass das Triebwerk einen Schub von 2,2 kN erzeugt und somit die angestrebte Leistung von 2,5 kN knapp verfehlt. Eine detaillierte Analyse des Strömungsfeldes offenbart eine unzureichende Vermischung der Treibstoffkomponenten in der Brennkammer, was zu Verbrennungsverlusten führt. Diese Beobachtung steht im Kontrast mit Testergebnissen von vorherigen Triebwerken des DeRisk-Projekts, wo die Parameter auf eine höhere Vollständigkeit der Verbrennung hinweisen. Dadurch wird die Frage aufgeworfen, ob das CFD-Modell in der Lage ist, die tatsächlichen Bedingungen des neuen Triebwerks akkurat darzustellen, und ob das neue Triebwerk in Tests ebenso gute Verbrennungseigenschaften aufweist, wie seine Vorgänger. Aus diesem Grund wird empfohlen, das CFD-Modell in zukünftigen Arbeiten weiter zu verfeinern und

Tests am neuen Triebwerk durchzuführen, um die Ergebnisse der vorliegenden und zukünftigen Simulationen zu validieren.

Contents

List of Figures

List of Tables

Nomenclature

Symbols

A_t	m^2	cross sectional area of the throat
c	m/s	velocity of the engine gases
c_e	m/s	effective velocity
E	J/mol	activation energy
F	N	Force
I_{sp}	m/s	specific impulse
k	-	reaction rate
k_d	m^2	Darcy coefficient
k_f	m	Forchheimer coefficient
L	m	sample thickness
$\dot{m}$	kg/s	mass flow rate
n	mol	number of particles
μ	kg/ms	viscosity
p	$\mathrm{N/mm^2}$	pressure
P_i	Pa	pressure at the inside of the combustion chamber
P_o	Pa	pressure on the cold gas side
P	Pa	pressure at the point of observation
R_S	J/kgK	specific gas constant
ρ	$\mathrm{kg/m^3}$	density
v	m/s	velocity
v_s	m/s	volumetric fluid velocity
v	$\mathrm{m^3kg}$	specific volume
V	m^3	volume
T	K	temperature
z	-	compressibility factor

Constants

R	8.314mol/molK	universal gas constant

Abbreviations

Fig.	Figure
Tab.	Table
CMC	Ceramic Matrix Composites
DSHT	Dual shell hyperboloid engine
HTP	high test peroxide

Explanation

O/F ratio	Ratio of oxygen to fuel mass flow in the rocket engine
Injector fuel mass flow	The percentage of the total engines fuel mass flow that is being injected into the combustion chamber through the injector

Introduction

In the wake of the global New Space trend, which is increasingly opening up space travel to private players, numerous start-ups and private space companies are emerging. In Germany, such examples are Rocket Factory Augsburg, Isar Aerospace, HyImpulse, and The Exploration Company. This change is creating a dynamic environment for the development of new technologies and applications. The DLR in Stuttgart has been conducting successful research into ceramic components for space travel at its Institute of Building and Structure (Institut für Bauweisen und Strukturtechnologie) for an extensive period of time. For example, the ceramic tip of NASA's X-38 was developed and built at the DLR. One innovative development by the DLR is the use of porous ceramics to create transpirative cooling films on surfaces. One application of this technology is the cooling of combustion chamber walls in rocket engines. Typically, the combustion chamber walls of rocket engines are regeneratively cooled by passing fuel through channels in the walls to the injector, which dissipates the heat generated by combustion and returns it to the combustion process by injecting it into the injector. In the DLR approach, the combustion chamber walls are porous, and fuel flows through the wall directly into the combustion chamber. This not only returns the heat from the wall to the combustion chamber but also blows off the boundary layer from the wall and forms a cooling film along the surface, which is why this approach offers clear advantages over conventional cooling of the combustion chamber wall. A further development of this technology is the use of a hyperboloid geometry for the combustion chamber. This so-called dual-shell hyperboloid engine geometry increases the wall surface area, thereby enhancing the beneficial effects of transpiration cooling. As these dual-shell hyperboloid engines are still a new development in the field of rocket propulsion, they have not yet been researched extensively. Black Engine Aerospace GmbH was founded as a spin-off from DLR to develop this technology further and make it available for the New Space sector. In its current KEROPEX project the goal is to develop a 2.5 kN engine that operates using kerosene as fuel and HTP as oxidizer. In the De-Risk phase of the KEROPEX project a sub-scale hyperboloid engine using kerosene and a mixture of hydrogen and oxygen to mimic the use of HTP has already been built and successfully tested. In this work, the CFD model of an existing 60-kN dual-shell hyperboloid engine powered by LOX/LCH_4, which has been thoroughly modeled in Ansys Fluent by [1], is used as a basis for downscaling it to the targeted 2.5-kN engine that runs on kerosene and HTP. The results of this CFD model are then compared to the simulation results of the 60 kN LOX/LCH_4 engine and to the test results from the De-Risk sub-scale engine, in order to verify the accuracy of the CFD model and determine the next steps for the CFD model as well as the entire KEROPEX project. [2], [3], [4], [5]

1 Theory

This section covers the most important fundamentals of rocket engines. First, the operating principle of rocket engines is discussed, and the various classifications of rocket engines are presented. This is followed by an introduction to dual-shell hyperboloid engines (DSHT) and their classification within rocket propulsion systems. The exact models of the predecessor engine from the previous work [1] and the new DSHT, which is discussed in this work, are also presented here.

1.1 Fundamentals of rocket propulsion

This section explains the operating principle of rocket engines and provides an overview of the existing engine classifications.

1.1.1 Thrust generation in rocket engines

Rocket engines operate according to the principle of reaction. This involves expelling the fuel carried by the rocket in the opposite direction to the direction of travel. According to the law of conservation of momentum, the momentum exerted on the expelled fuel acts in the opposite direction—i.e., in the direction of travel—on the rocket, thereby propelling it forward. There are essentially two ways to increase the momentum and thus the thrust of the rocket:

- **Mass Flow Rate:** A larger quantity of propellant is expelled per unit of time (mass flow rate $\dot{m}$).
- **Exhaust Velocity:** The propellant is expelled at a higher velocity (v_e).

Figure 1.1 schematically illustrates how the momentum theorem is applied to a rocket.

Figure 1.1: Schematic of the momentum theorem on a rocket

For the design and evaluation of rockets, the thrust F and the specific impulse I_{sp} are mostly considered. Before looking at these, it needs to be added that the illustration in figure 1.1 applies when the rocket has no atmosphere around it. Then the thrust consists of only the impulse component. When there is an atmosphere surrounding the rocket, the thrust has an impulse component and a pressure component. The thrust results in:

$$F = \dot{m} \cdot \tilde{v}_e + (\tilde{p}_e - p_a)A_e = \dot{m}c_e, \tag{1.1}$$

where $\dot{m}$ is the mass flow, $\tilde{v}_e$ is the mean exit velocity of the gases over the exit plane of the engines expansion nozzle, $\tilde{p}_e$ the mean exit pressure of the gases over the exit plane, and p_a the ambient pressure. The thrust can also be described as a multiplication of the mass flow $\dot{m}$ and the effective velocity c_e. If the expansion nozzle is adapted to the surrounding pressure, then the term $(p_e - p_a)$ equals zero. In this case, the thrust only consists of an impulse component, and c_e equals v_e. While the thrust is an excellent measure for the power of a rocket engine, it is difficult to evaluate the efficiency of two engines that use the same fuel but differ in their thrust class. The specific impulse solves this problem by relating the thrust of an engine to its mass flow and Earth's gravitational constant:

$$I_{sp} = \frac{F}{\dot{m}g} = \frac{c_e}{g}. \tag{1.2}$$

This way, the efficiency of the engine is given in seconds. The higher the specific impulse, the more thrust per kilogram of fuel can be generated. [6]

1.1.2 Classification of rocket propulsion systems

Over time, various types of rocket propulsion systems have been developed, each implementing the recoil principle in different ways. The following provides an overview of the most important operating principles. Rocket propulsion systems can be classified in various ways, for example, by the thrust they generate, the state of the propellant used (liquid, solid, hybrid), or the energy source used to implement the recoil principle. The latter criterion is used for the classification here. [6]

Chemical rocket propulsion systems

Chemical rocket propulsion systems use chemical energy in the form of an exothermic reaction to expel their propellant. This reaction causes a significant increase in pressure and temperature of the gases in the combustion chamber. The hot gases are then expanded and accelerated through a Laval nozzle. A subsequent expansion nozzle further accelerates the gases to maximize thrust. Chemical rocket engines can be further divided into three categories:

- **Solid rocket engines:** Fuel and oxidizer are mixed together in solid form. They are stored in a vessel that is both the tank and combustion chamber at the same time. Once ignition has taken place there is no way for active control of the burning rate or even a stop and later reignition. However, solid rocket motors are simple in their design and easy to handle.
- **Liquid rocket engines:** Fuel and oxidator are in liquid form, stored in separate tanks that are also separated from the combustion chamber. The fuel and the oxidizer need to be pumped into the combustion chamber for combustion. Pumps, pipes and valves are needed for this as well as often times preburners, that burn some of the fuel and oxidizer to generate the power to run the pumps. The combustion chamber is also significantly more complex than in solid rocket motors. On the upside, this engine can throttle its thrust, be reignited and also vary its mixing ratio, which allows for much more versatile use.
- **Hybrid rocket engines:** One of the components is in solid form and the other in liquid form. Often times the solid component is stored in the combustion chamber and the liquid component can be injected in a cotrolled manner so that the engine's thrust can be controlled and the engine can be even reignited. Depending on the configuration the characteristics of both liquid and solid rocket engines can be combined.

The dual-shell hyperboloid engine presented in this work is also a chemical rocket engine and belongs to the liquid rocket engines. [6]

Electric rocket propulsion systems

In electric rocket propulsion systems, energy is supplied to the propellant not through an exothermic chemical reaction but through electrical energy. There are several approaches to this, which is why electric rocket propulsion systems can be classified into further subgroups:

- **Electrothermal thrusters:** The propellant is heated in the "combustion chamber" by electrical energy and then expanded through a Laval and expansion nozzle.
- **Electrostatic thrusters:** These thrusters ionize particles and expel them by acceleration using electric fields (e.g., ion thrusters).
- **Magnetoplasmadynamic thrusters:** Here, the Lorentz force of electric arcs is used to accelerate ions.

Electric propulsion systems are characterized by a significantly higher exhaust velocity of the propellant but generate less thrust than chemical thrusters. As of today, electric propulsion systems are not suitable as main engines for launch vehicles due to their low thrust. However, as orbital thrusters, they can achieve higher final velocities than chemical thrusters with a sufficiently long operating time. In summary, chemical propulsion systems are velocity-limited, while electric propulsion systems are thrust-limited. [6]

Nuclear rocket propulsion systems

Nuclear rocket propulsion systems use energy released by nuclear fission–or fusion (potentially in the future)–to heat their propellant and expand it through a Laval and expansion nozzle. This allows for potentially very high exhaust velocities and thus high specific impulses. [6]

1.2 The dual-shell hyperboloid engine

Classic liquid rocket engines are designed in a cylindrical Laval nozzle configuration, as shown in Fig. 1.2. The combustion chamber is cylindrical in design. Fuel and oxidizer are injected into the chamber via an injector (shown on the left end), where they mix and react. The temperature and pressure increase, and the gases flow down the combustion chamber. Combustion in rocket engines occurs at extremely high temperatures exceeding 3,000 K, generating large amounts of heat. This results in significant heat flow through the combustion chamber wall, throat, and nozzle. To dissipate this heat, these engines are usually cooled regeneratively. The combustion chamber walls, the nozzle throat, and—depending on the engine—even sections of the expansion nozzle are double-walled. A fuel component is fed through channels in the walls. It absorbs the thermal energy from the wall and feeds it back into the combustion chamber via the injector. This recovered heat increases combustion efficiency. It is why it is referred to as regenerative cooling. The combustion chamber tapers to a narrow cross-section at its end, which is also known as the nozzle throat. This transition is quite rapid, not gradual. In this section, the gases relax and accelerate. In the nozzle throat, the flow reaches a speed of Mach 1. The contour then transitions into the expansion nozzle, where the gases are further relaxed and accelerated. The exit plane, which marks the end of the expansion nozzle and the engine, represents the transition to the environment. This design is the most common for liquid rocket engines, but it has some disadvantages both in terms of the way of cooling and the contour shape. Sarting off with the cooling: if the walls of the engine could be made porous, the efficiency of regenerative cooling could be increased by allowing the fuel component used for cooling to be diffuse through the walls from the outside directly into the combustion chamber, thereby also returning the heat from the

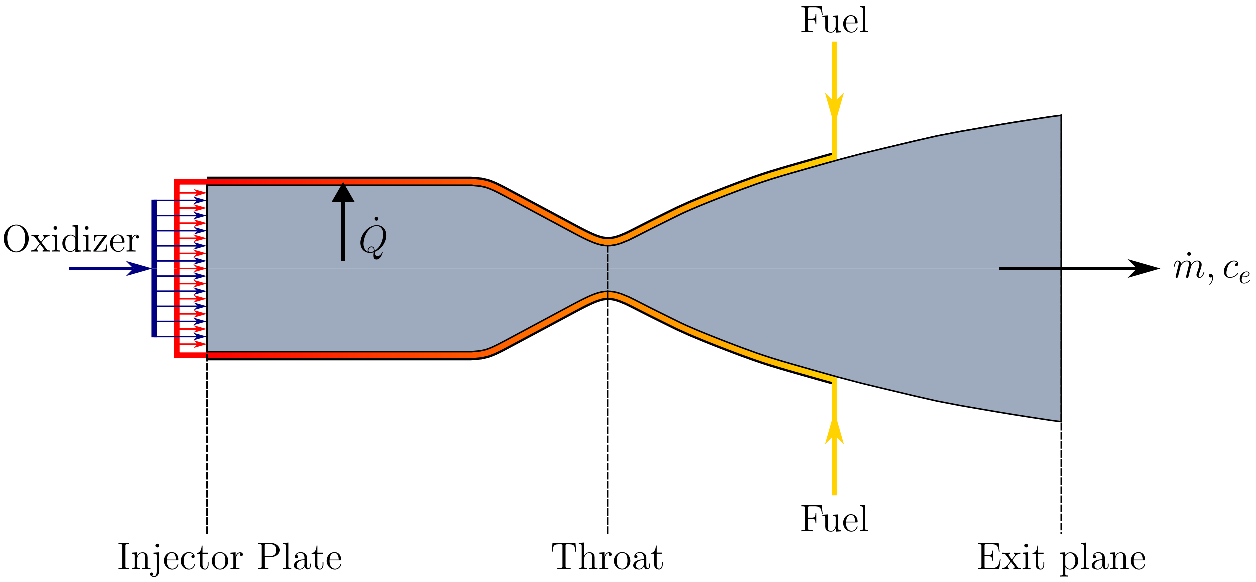

Figure 1.2: Schematic representation of the functioning and regenerative cooling of a conventional liquid rocket engine with a cylindrical combustion chamber

walls directly to the combustion chamber. In this way, injection and cooling are combined. More aspects are coming up. Blowing the gas through the wall creates a cooling film between the hot gas flow and the wall, as shown in figure 1.3. This results in two additional advantages. Firstly, the hot gas flow does not come into contact with the surface roughness and is slowed down less. This means that the boundary layer is less pronounced, resulting in less flow resistance and turbulence. Secondly, heat conduction through contact between the hot gas flow and the wall is primarily prevented, reducing the heat input into the walls. The first approach of the DLR and

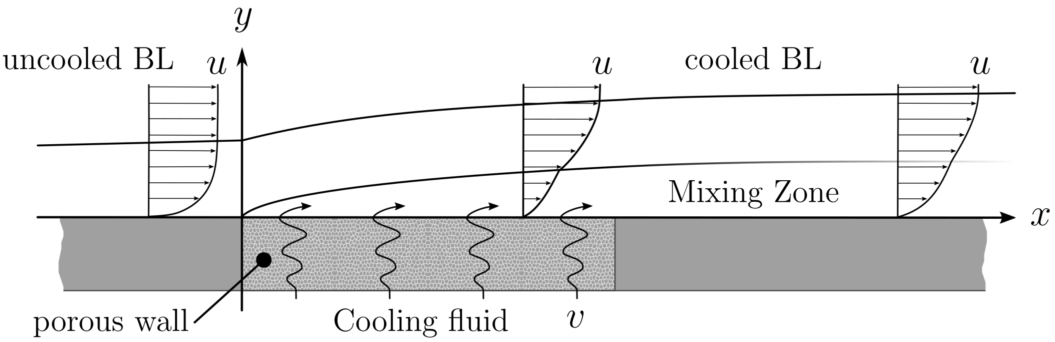

Figure 1.3: Schematic representation of the transpiration cooling process [7]

BEA was, then, to build a rocket engine with the classcial cylindrical combustion chmaber shape and to replace the traditional regenerative cooling with the transpiration cooling as shown in figure 1.4. The next step was to modify the shape of the combustion chamber. On the one hand the effects of the transpiration cooling should be maximized. On the other hand the transition to the nozzle throat should be modified to be more gradual in order to minimize disturbances to the flow. To maximize the effects of the transpiration cooling the surface area of the combustion

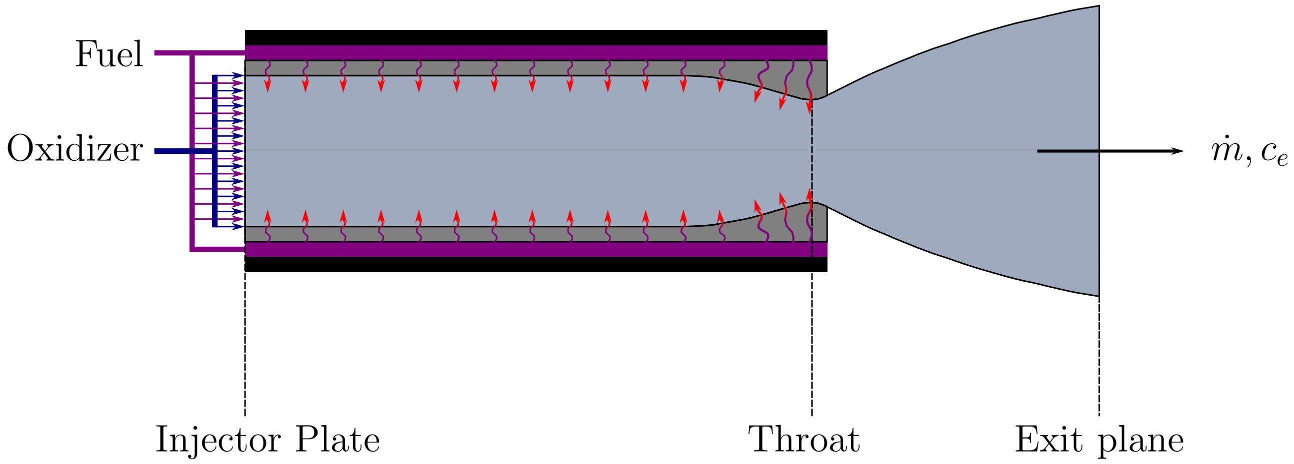

Figure 1.4: Schematic representation of the functioning and transpiration cooling of the first design iteration at BEA and the DLR on a conventional liquid rocket engine with a cylindrical combustion chamber but with porous CMC combustion chamber walls for transpirative cooling.

chamber needed to be increased. The contour of the wall was changed from a cylinder to that of a single-shell hyperboloid. Them another contour was added with an internal dual-shell hyperboloid inside the combustion chamber. Now there were two contours to the combustion chamber. A gap with a ring-shaped cross section forms between those contours. This gap represents the interior of the combustion chamber. Only this gap is flowed through (no combustion or anything else takes place inside the inner hyperboloid). Both the outer and inner hyperboloids taper in the direction of flow. This occurs in such a ratio that the cross-sectional area of the gap remains constant, hence the cross section imitates the behavior of the cross section of a cylindrical combustion chamber. At a certain point, the inner hyperboloid ends. From here, the outer hyperboloid continues to taper toward the nozzle throat. This section is equivalent to that of an engine with a cylindrical combustion chamber, but as already mentioned there the taper is very abrupt and the resulting contour has a strong S-curve. This causes strong flow deflections. These are associated with losses and cause increased turbulence in the boundary layer and thus high heat load peaks near the wall at the throat. This results in higher erosion rates in the throat. The flow resistance in this area is also not insignificant. In the dual-shell hyperboloid engine, this transition in the combustion chamber to the nozzle throat is more gradual and there is no S-curve, as in the cylindrical engine. The flow is deflected less aggressively, resulting in fewer losses, less turbulence in the boundary layer, and thus lower heat load peaks and erosion in the nozzle throat. This geometry with smoother transitions reduces flow resistance in the transition to the nozzle throat, allowing the nozzle throat to be made smaller for a given mass flow and combustion chamber pressure, which can be used to reduce the weight of the nozzle and increase the flow velocity. A schematic of the resulting dual shell hyperboloid engine is depicted in figure 1.5. Another advantage of the engine is anticipated here. The porous walls of the combustion chamber are not part of the engine housing. The housing is a separate metal structure surrounding the porous walls. The loads of the engine

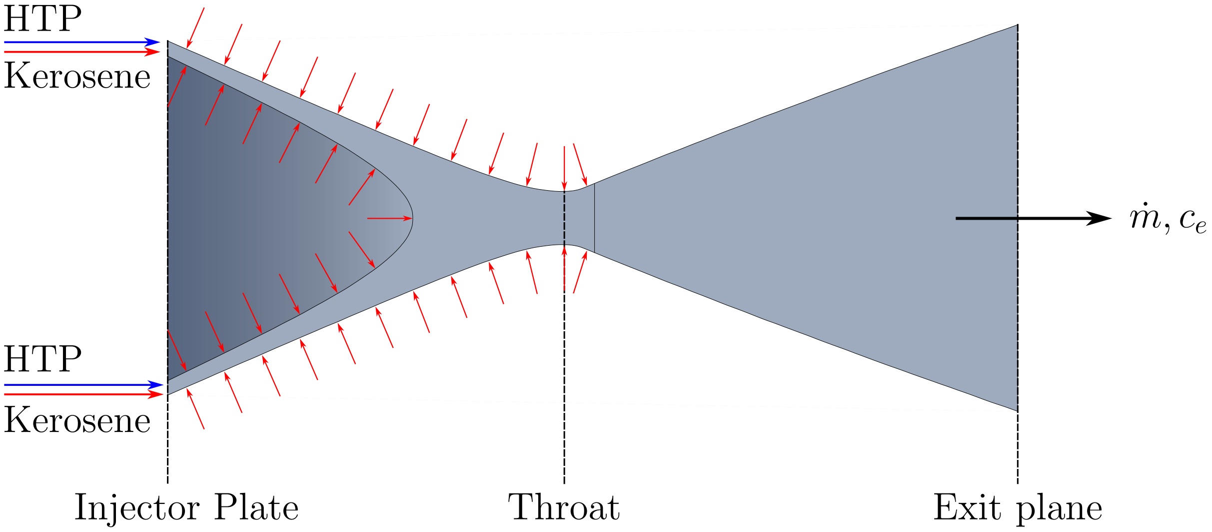

Figure 1.5: Schematic representation of the dual-shell hyperboloid engine

are carried by the metal housing. The porous walls of the combustion chamber are decoupled from these loads. This results in a considerable reduction in fatigue, which offers a significant increase in service life compared to state-of-the-art engines with a cylindrical combustion chamber design. [2], [3], [4], [5]

1.3 Performance scaling

At the start of this work, the geometry of the 60 kN engine has arleady been physically scaled to the geometry of a 2.5 kN engine with regard to the use of HTP and kerosene. This work delivers the simulative part of the scaling process and the relative classification of its results in relation to the simulation results of the 60 kN LOX/LCH_4 and the test results of the De-Risk engine. In this section information about the 60 kN LOX/LCH_4 engine is given first and then some infromation about the physical scaling and the final design of the 2,5 kN kerosene/HTP engine.

1.3.1 The 60 kN LOX/LCH_4 engine

The predecessor engine of this work is a DSHT with 60 kN thrust, which uses methane (CH_4) as fuel and oxygen (O_2) as oxidizer. The injector has a hole pattern through which the methane and oxygen flow. For transpiration cooling, part of the hydrogen flows through the porous walls. In the simulations from [1], vacuum thrusts of up to 66.5 kN were achieved for the engine. This is close to the theoretical values of 66.14 kN, which were determined using NASA RPA. To illustrate the size of the engine: the combustion chamber has a length of 439.84 mm, and the radius of the outer contour at the injector plane is 113.25 mm.

1.3.2 The 2,5 kN HTP/Kerosene engine ASSY R5

This section is split up into three subsections. The first covers some information about the physical scaling of the engine. The second one introduces the injector plate design since it will be crucial for the CFD model and the third shows a view of the full engine design.

1.3.2.1 Peliminary design of the engine parameters

The basis of every rocket engine design is a preliminary design. This is where the required mass flows, as well as the dimensions of the combustion chamber, throat, and expansion nozzle, are determined. The preliminary design has been performed with NASA's CEA (Chemical Equilibrium with Applications) program. It was developed by NASA to solve combustion and rocketry problems by calculating chemical equilibrium compositions and thermodynamic properties of complex mixtures, and it has been in development since the 1940s. Table 1.1 lists the most important parameters going into the preliminary design.[8]

Table 1.1: Initial parameters for the preliminary design with CEA

Thrust (vacuum)	2.5 kN
Chamber pressure	20 bar
O/F ratio	7
Fuel	Kerosene
Oxidizer	Hydrogen peroxide

These parameters yield the following mass flows for kerosene and hydrogen peroxide

$$\dot{m}_{\text{Kerosene}} = 0.102 \text{ kg/s and } \dot{m}_{\text{Hydrogen peroxide}} = 0.719 \text{ kg/s} \tag{1.3}$$

which leads to an oxidizer to fuel ratio of

$$\frac{\dot{m}_{\text{Hydrogen peroxide}}}{\dot{m}_{\text{Kerosene}}} = 7.049. \tag{1.4}$$

Since kerosene is a combination of various hydrocarbon chains, and there is no exact definition of one kerosene, the stoichiometric ratio with another oxidizer cannot be determined precisely. Based on kerosene as an accumulation of $C_{12}H_{23}$ chains, the above mass flows result in a stoichiometric mixing ratio of 7.217. The acquired O/F ratio from 1.4 is lower than that, which means that it presents a fuel-rich mixture.

Injector plate design

Since the injector plate only has to carry one medium, its design is easier to implement. A slot pattern consisting of 36 slots with a thickness of 0.6 mm and a width of 20° is used. The pattern repeats every 30°. Figure 1.6 shows the injector plate with the injector pattern. A 30° section is marked, showing which section was used for modeling (more on this in chapter 2.1.1). It should be noted that the pattern is periodic and cannot be mirrored at any point.

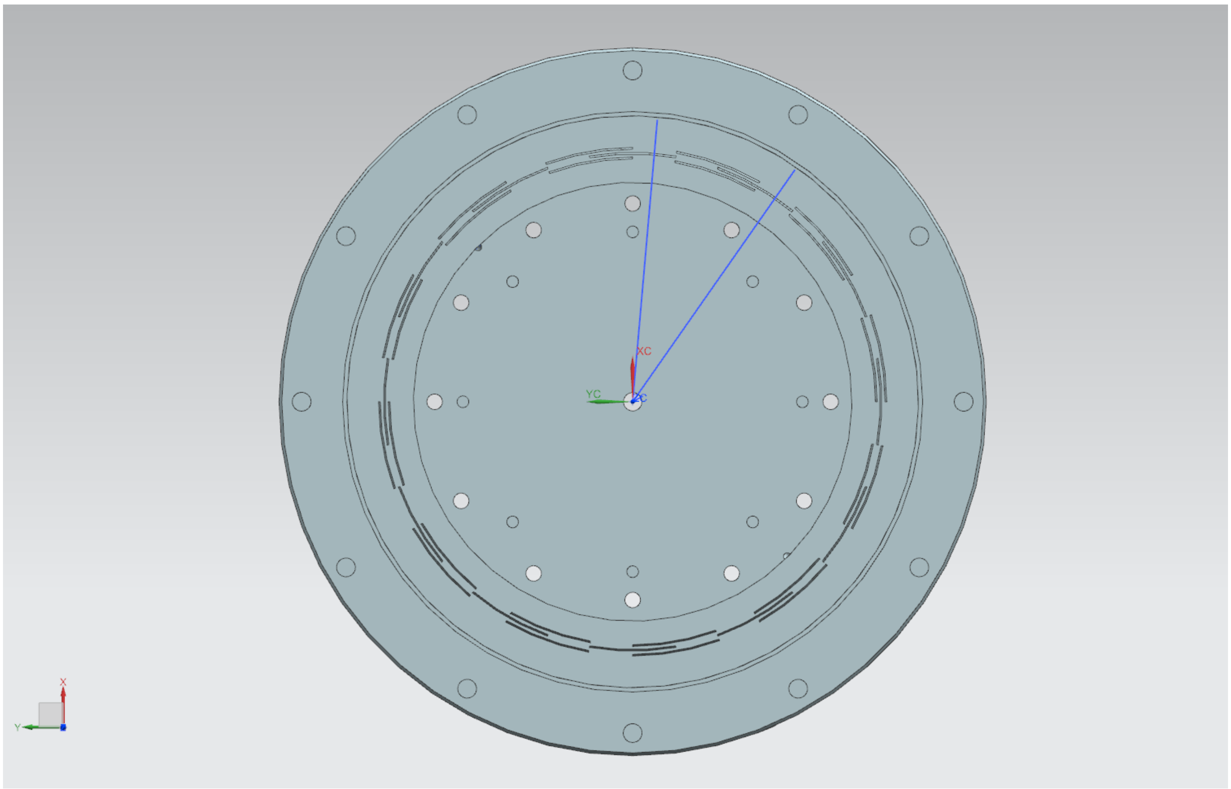

Figure 1.6: View of the injector plate in a CAD program. Two blue lines indicate the section taken for modeling in the CFD.

The finished rocket motor

Finally, an overview of the finished engine should be given. The design of the combustion chamber, the nozzle neck, the expansion nozzle, and the pattern on the injector plate results in the following overall design:

The outer combustion chamber contour is designed as a porous wall from the injector to behind the throat. The inner contour is designed as a porous wall starting from the injector and features a graphite tip that is not porous and does not enable transpiration cooling. Another injector for the hydrogen peroxide is located at the foremost part of the inner body. However, on the instructions of the contractual partners of this project, this smaller injector should not be simulated and is therefore not considered further in this elaboration.

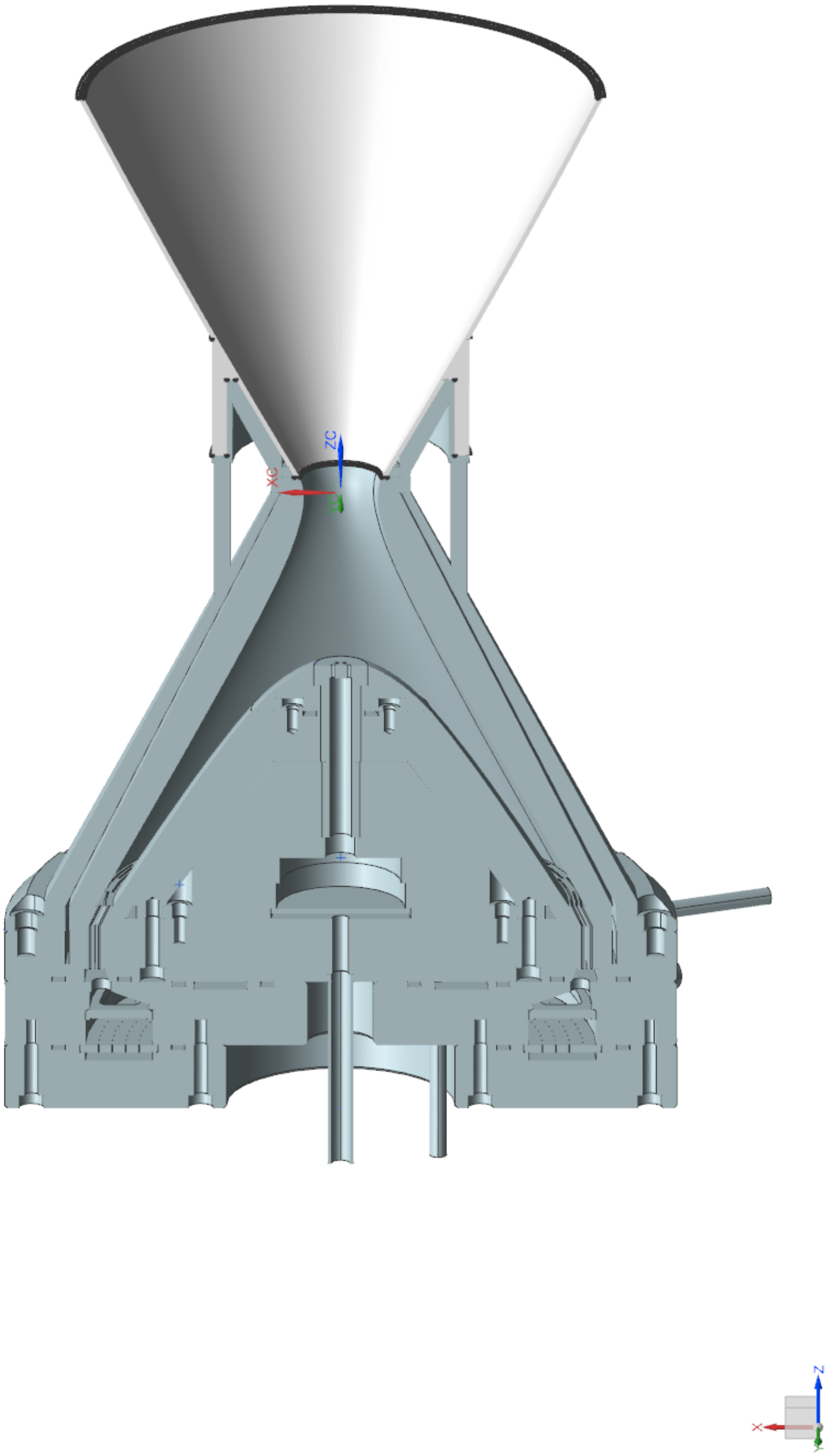

Figure 1.7: View of a cut of the final engine in a CAD program.

2 Methodology

The following section explains in more detail the methodological approach of this work, which particularly covers the modeling of the engine's flow simulation. The evaluation of the simulations results and their comparison to the results from the De-Risk sub-scale variant tests are covered in the results chapter.

2.1 Model building and simulation setup

The design and parameters of the engine are followed by the modeling process. This will be described in the following sections. The CFD tool *Fluent* from *ANSYS* version 2024 R2 was used for the simulation. To begin with, an overview of the case that is to be simulated and the simulated domain is provided. This is followed by a presentation of the boundary conditions and an explanation of the models used.

2.1.1 Overview and domains

In this work a model for the combustion and flow processes inside the combustion chamber, the nozzle throat, and the expansion nozzle is established. Processes in the injector, ducts, etc. are not considered. The case considered is that of the engine operating at full power and in its environment as an upper stage engine. Therefore, a near-vacuum is assumed. Gravitational effects are neglected, as this reduces the computing power required (more on this in chapter 2.1.3) and the gravitational force would not be known anyway, since in this case the engine will already have built up a considerable part of its orbital velocity around the Earth, thus compensating for the gravitational force to a certain extent. The environment surrounding the engine is also not modeled, as this would require more computing power and would not influence the flow within the engine (more on this in chapter 2.1.3). Since the engine is rotationally symmetric and the injector pattern repeats along the circumferential direction, exactly the same conditions occur in each section in which the injector pattern repeats. Thus, the entire domain can be represented by one of these sections, which has a periodic boundary condition at the interfaces to the other sections (more on this in chapter 2.1.3).

2.1.2 Computational mesh

The meshes were created using the *ANSYS Meshing* tool. The mesh has a significant influence on the accuracy, convergence behavior, and speed of the simulation. Therefore, a mesh study with several meshes with varying configurations had to be carried out in order to determine a mesh configuration that generates the most accurate and physically meaningful solution possible, while keeping the computational effort within the scope of this work. The basis of the meshes was an unstructured mesh of tetrahedra with a global element size of 3 mm. In order to resolve the boundary layers of the flow in the engine, prismatic layers were created on the walls. Here, the first layer thickness method was applied, with an initial thickness of 0.01 mm, a layer count of

25, and a growth rate of 1.2, based on [1]. Since the free flow must be finely resolved, especially in the combustion chamber gap and in the nozzle throat, the wall surfaces of the outer liner and the entire inner hyperboloid body were provided with a finer surface mesh. This was adjusted so that the volume adjacent to the surfaces is also refined. This allowed the entire area from the combustion chamber gap to behind the nozzle throat to be meshed more finely. Since the injector itself is not modeled, the adjacent openings of the injector are modeled as surfaces at the injector level of the mesh. The inlets of the injector were meshed with a fineness of 0.1 mm. Figure 2.1 shows an example of a section of one of the grids used. The differences lie in the varying fineness of the grid—the exact configurations of the grids are described in the results chapter 3.1.

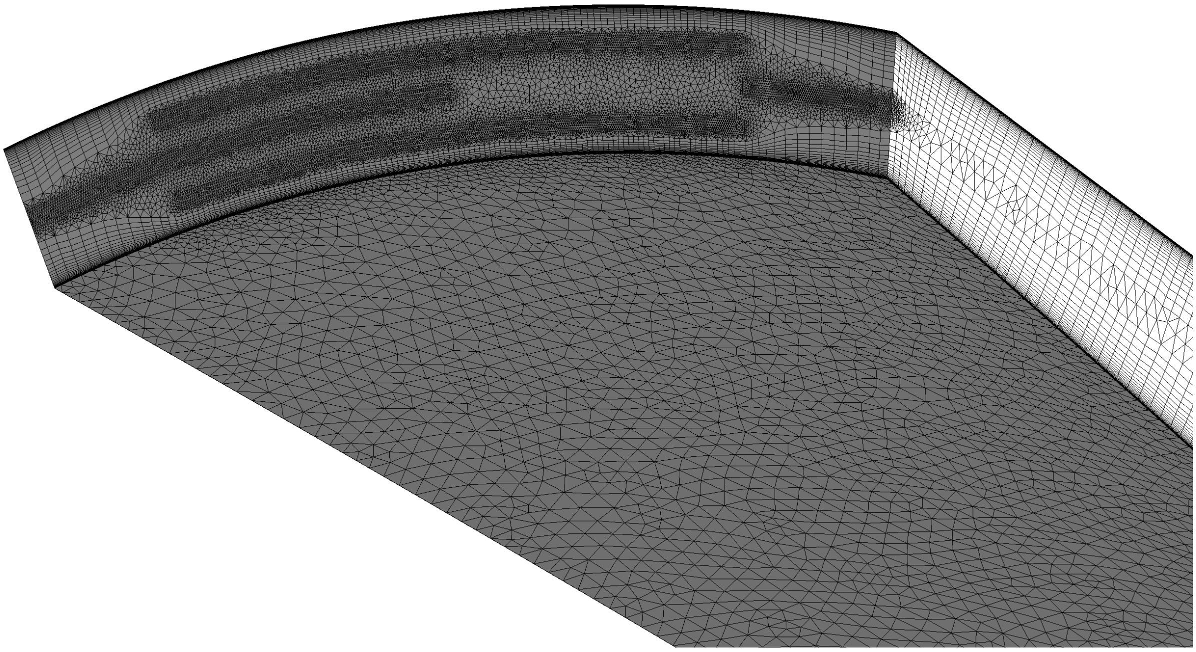

Figure 2.1: Front view of one of the computational meshes used at the injector plate with an element size of 1 mm in the combustion chamber, prism layers with a thickness of 0.01 mm for the first layer, 25 layers and a growth rate of 1.2, and a surface cross-linking of 0.1 mm at the injector inlets.

2.1.3 Boundary Conditions

The boundary conditions of a numerical simulation have a significant influence on the convergence behavior and physical plausibility of the results (see section 3.2). They must therefore be selected in such a way that the calculation converges stably and the modeling and results reflect the real world physically correctly.

Inlet

A mass flow boundary condition is set at the injector openings. The mass flow was adjusted proportionally to the size of the engine section. The inflowing medium is decomposed hydrogen peroxide. Its composition prior to decomposition was specified as 95 wt.% hydrogen peroxide and 5 wt.% water. The ratio of water to molecular oxygen resulting from decomposition was taken into account accordingly. Another obligatory specification was an inlet temperature of 1144 K resulting from the decomposition. The inflow pressure was set to the combustion chamber pressure of 20 bar. The channels of the physical injector are not aligned along the axis of symmetry of the engine, but along the inner contour of the engine. This can also be seen in Figure 1.7 at the inlet of the combustion chamber. This results in an inlet vector that is inclined at 30° to the axis of symmetry of the engine. Since only the openings to the combustion chamber are modeled as inlet surfaces for the injector, the resulting inflow vector was entered manually using cylindrical coordinates. The modeling of the kerosene inlets was implemented and tested using three variants. One as **mass flow inlets**, the other as **velocity inlets** and the third as a special variant where the whole **CMC liners** were **modeled as flow domains**. More on this and the third variant in chapter 2.1.5.

Outlet

The computational domain ends at the outlet of the expansion nozzle, as the environment surrounding the engine is not simulated. A pressure boundary condition is set at this exit level. This choice is particularly suitable, as the ambient pressure is relevant for rocket engines because it can influence the flow pattern in the expansion nozzle and in the wake. Another advantage of the pressure boundary condition is that it allows the flow to develop naturally, in contrast to a mass flow boundary condition. In earlier simulations, the latter was set to the exact mass flow of the engine. Since there was excess gas in the computational domain at the start of the simulation due to initialization, which could not escape, gases were accelerated from the nozzle throat but slowed down again due to buildup in the expansion nozzle. The pressure boundary condition, on the other hand, allows excess gas to escape, causing the flow to converge stably. However, the pressure boundary condition is only relevant during the initialization of the simulation. Since a supersonic flow develops in the nozzle, pressure conditions cannot propagate upstream. The pressure at the exit plane, therefore, only influences the flow if it is higher than the pressure that would naturally develop at the nozzle outlet (for more information, see chapter 3.2).

Periodicity

As already mentioned in Chapter 2.1.1, the combustion chamber is rotationally symmetric and the injector repeats every 30°, resulting in numerically identical conditions every 30° in the circumferential direction. The computational effort can be significantly reduced by simulating the flow in only one section. For this purpose, a 30° section is taken from the domain. The interfaces where the 30° section adjoins the others are provided with periodic boundary conditions. The flow conditions that leave one of these periodic surfaces re-enter through the other side. The surface mesh is identical on both periodic surfaces. This means that each cell on one of the periodic surfaces fits exactly onto a cell on the opposite surface. In this way, the cells do not overlap, the flow conditions do not have to be interpolated between several cells, and the computational effort is kept low. Since the injector pattern repeats every 30°, but each 30° section is not symmetrical in itself, it can be assumed that flows with asymmetrical circumferential components can form due to the injector pattern. It is therefore important that the boundary condition at the intersection surfaces is truly periodic and not mirroring.

Walls

All other surfaces are designed as walls. The wall roughness of the expansion nozzle and the graphite tip is set at 10 μm. This is based on information provided by the manufacturer Inovaceram for the expansion nozzle and by the manufacturer TVB for the graphite tip. No roughness data is available for the injector. Its surface roughness is considered negligible, as the flow essentially flows away from it perpendicularly. The surface of the CMC liners at the cooling flow inlets is negligible, as the injection of kerosene through the surface assumes that the boundary layer in this area is blown away. Thus, no boundary layer is created in this sense. For the evaluation of the simulations, the heat flows through the walls are also considered, among other things. Here, the focus is on how the heat flows differ from simulation to simulation. In order for Ansys Fluent to calculate these heat flows, and since the heat coefficients are not known, fixed wall temperatures are assigned to the walls. To ensure that the heat flows only differ from simulation to simulation due to other conditions, each wall must be assigned the same wall temperature in each simulation. Since no empirical data is available, for simplicity's sake, all walls were assigned the same temperature of 300 K.

2.1.4 Gas modeling

Species

Ansys Fluent comes with a wide range of materials pre-installed. Since the hydrogen peroxide enters the combustion chamber already decomposed, the oxygen (O_2) and "water vapor" options were selected in Ansys for the modeling. As mentioned in Chapter 1.3, kerosene is a composition of several hydrocarbon chains, and modeling multiple complex molecules, especially when modeling reactions, significantly increases the computational effort. Therefore, kerosene was modeled using a surrogate fuel consisting of only one hydrocarbon chain. However, it was selected so that it would enable the most realistic modeling of kerosene possible. The option "kerosene-vapor (c12h23)" was selected for this purpose (more on this in the section "Combustion Model"). The material properties are already stored for the respective materials. The heat capacity is stored for all materials using polynomials for temperatures up to 5000 K.

Gas model

To determine the gas model, the compressibility factor of the individual substances was examined. The compressibility factor allows an estimate to be made as to whether a gas behaves like an ideal gas under given conditions. It results from converting the ideal gas equation $pV = nRT$ to the following form,

$$z = \frac{pV}{nRT} = \frac{pv}{R_S T} \tag{2.1}$$

where p is the static pressure, V is the volume, v is the specific volume, T is the temperature, and R is the universal gas constant and R_S is the specific gas constant, which is obtained by relating the universal gas constant to the molar mass of the gas in question. With a compressibility factor of one, the gas in question behaves like an ideal gas. The individual substances were examined for their compressibility factor in the combustion chamber. The NIST database provides a large number of data points for this purpose. For oxygen, water, and carbon dioxide, the values for pressures from 20 bar were stored for up to 2000 K. The compressibility values of these substances were then determined at 20 bar for temperatures of 1000 K and 2000 K (see tab 2.1). The values

Table 2.1: Compressibility factors of oxygen, water vapor, and carbondioxide at a pressure of 20 bar

Species	Compressibility factor at	
	1000 K	2000 K
Oxygen	1.00507	1.00314
Water vapor	0.995141	1.00104
Carbon dioxide	1.0041	1.0041

for all three substances are approximately one. The substance values are only stored in the NIST database up to 2000 K, which is why no evaluation could be carried out up to 3000 K. Since the compressibility factor already assumes values of almost exactly one at the expected pressure at 2000 K, it is assumed that it will also be one at a temperature of 3000 K. When considering the compressibility factor, kerosene could not be taken into account because no values for it were stored in the NIST database. The evaluation for this remains pending. It can be assumed that the vapors of kerosene deviate from the behavior of an ideal gas due to its long-chain molecules. Since this work is a preliminary consideration and the substances that exhibit the behavior of an ideal gas predominate in the combustion chamber, the media are modeled as ideal gases in the simulations.

2.1.5 Implementation of the transpiration cooling

There is no suitable boundary condition in Ansys Fluent for implementing transpiration cooling. To physically model transpiration cooling in its entirety, the CMC liners would need to be implemented as porous domains, with the fuel entering in liquid form on the cold gas side, flowing through them, and exiting on the hot gas side in the combustion chamber. As it flows through the wall, the fuel absorbs heat transferred to the walls as thermal radiation from the combustion. In the process, the fuel undergoes a phase change while still in the porous wall. It would then enter the combustion chamber on the hot gas side and blow off the boundary layer from the surface. This would prevent the cooling mass flow from coming into contact with the walls, which would cause friction and the formation of a boundary layer. It would also prevent heat from being transferred to the liner walls in the form of conduction through contact with the free flow. The modeling of the liner as a porous domain, the flow of fuel through it, the phase change in the porous domain, and the modeling of heat transfer into the porous domain can all be modeled. However, a complete model is so complex and computationally intensive that it far exceeds the scope of this work. A simpler variant must be found. In the previous work by Hoffmann [1], the surfaces of the porous liners were defined as walls, and source terms for the mixture fraction were added to the first layer of cells above them to simulate the entry of the fuel. This approach is attractive because it preserves the surface of the liners as a wall, allowing heat flows into the wall to be determined, but a simpler approach was chosen.

The CMC liner surfaces are defined as inlets. In Ansys Fluent, for example, mass flow and velocity inlets are available. In both variants, the surface of the liners is not designed as a wall, but as a boundary. In the case of the mass flow inlet, the mass flow flowing through this boundary is set as a hard condition. Other parameters, such as the specified pressure and temperature of the incoming fuel and the prevailing flow conditions, determine its inlet velocity. With the velocity inlet, on the other hand, the velocity is set as a hard boundary condition, and the mass flow is calculated as a result of all other conditions. Ultimately, both variants should arrive at the same result via different paths. However, since mass flows are a fundamental parameter in rocket propulsion, it is far more practical to choose the mass flow boundary condition, as it always exactly implements a specified mass flow. With a velocity inlet, the parameters must be adjusted iteratively to achieve the appropriate mass flow. This process is cumbersome and time-consuming, especially when other engine parameters change and, in turn, influence the resulting mass flow. Due to this disadvantage, the mass flow inlet is preferred over the velocity inlet, but both variants are compared by numerical experiment (see chapter 3.4). The desgin from Table 1.1 specifies a combustion chamber pressure of 20 bar. In previous engine tests at Black Engine Aerospace GmbH using kerosene as the cooling medium, temperatures of 400°C were measured on the liner surface. This value was specified as the temperature for the cooling mass flow inlets.

2.1.6 Turbulence model

The commonly used $k-\omega-SST$ model was used as the turbulence model. It combines the advantages of the $k-\omega$ model near walls and the $k-\epsilon$ model in the free-stream region by linearly combining the two models via a mixing function [9]. This continuous mixing ensures that the accurate results of the $k-\omega$ model near the wall and the robust results of the $k-\epsilon$ model in the free-stream region are utilized, making the model a very reliable tool.

2.1.7 Combustion model

The numerical modeling of kerosene combustion poses a particular challenge. Compared to the combustion of pure fuels, such as LOX/CH_4 combustion in the 60 kN engine, which could be modeled relatively easily, kerosene is not a single chemical compound. Instead, it is a mixture of a large number of long-chain hydrocarbons, the exact composition of which varies. Detailed mapping of the chemical kinetics is therefore complex and requires enormous computing power. A one-step reaction mechanism is, therefore, used for the initial scaling of combustion in this work. The choice of this simplified approach is based on the study by Zeng et al. [10]. In their study, the authors first developed a new, reduced chemical-kinetic mechanism for n-decane, which serves as a surrogate fuel for kerosene. This complex model comprises 50 species and 210 elementary reactions and was validated using ignition delay times in a shock tube at pressures of 12 bar and 50 bar. Since the operating pressure of 20 bar used in this work is within this validated range, the study is considered a relevant reference. The decisive factor in the choice of model is the comparison made by Zeng et al. between their detailed mechanism and a global one-step reaction. They found that the results of both models show only a slight discrepancy. The global reaction equation used is:

$$\mathrm{C_{12}H_{23}} + 17.75\,\mathrm{O_2} \longrightarrow 12\,\mathrm{CO_2} + 11.5\,\mathrm{H_2O} \tag{2.2}$$

The reaction rate k is calculated using the Arrhenius formula

$$k = Ae^{-\frac{E}{RT}} \tag{2.3}$$

for which the following parameters are specified: a pre-exponential factor $A = 2.587 * 10^9$, a temperature exponent $\beta = 0$, and an activation energy of $E = 1.257 * 10^5 J/mole$. Furthermore, e is Euler's number, R is the universal gas constant, and T is the absolute temperature in Kelvin. The modeling was implemented accordingly using the Species Transport Model in Ansys Fluent. However, it should be noted that the study by Zeng et al. focuses on combustion in an aircraft engine, in which nitrogen from the air plays an essential role. The rocket engine considered here, on the other hand, burns kerosene with the decomposition products of hydrogen peroxide (oxygen and water vapor), which is why nitrogen is not present in the system. Since the kinetic parameters of the one-step model used by Zeng et al. are potentially tailored to the presence of nitrogen, even though nitrogen itself does not appear in the reaction equations, certain deviations in the results of the present simulation are to be expected. Nevertheless, the approach represents a valid and computationally efficient method for an initial analysis.

2.1.8 Solver

Ansys Fluent offers both a pressure-based and a density-based solver for performing flow simulations. Traditionally, the density-based solver is recommended for compressible flows at high Mach numbers, while the pressure-based solver is primarily used for incompressible or low-compressible applications. There is some literature that has investigated both variants in different Mach regimes extensively and concludes that the pressure-based solver delivers results comparable to those of the density-based solver and experimental data, while exhibiting higher numerical stability and faster convergence than the density-based solver [11], [12]. A publication by Ansys also mentions that the pressure-based solver can be used up to a Mach regime of 4, which should be within the scope of the application in this work [13]. Based on these findings, the advantages in terms of stability and convergence, and since the pressure-based solver has already been used successfully in previous work [1], it is also the preferred choice for the present simulation.At this point, the information is provided that the pressure-based solver has demonstrated significantly higher numerical stability in this work compared to the density-based solver.

3 Results & Discussion

The results of the modeling of the 2.5 kN dual-shell hyperboloid engine are presented in this chapter. First, a mesh study is performed to ensure that the mesh does not influence the simulation results. This is followed by an observation of how the pressure boundary condition at the exit plane affects the simulation results. The flow pattern of the engine is then examined in detail, and an overview of the engine and all occurring flow phenomena is given. Subsequently, the implementation of the transpiration cooling is examined and discussed in more detail. The combustion model is then examined in more detail, anticipating the engine's performance parameters, which are compared to those derived from NASA CEA calculations.
In the course of this work, another design for the injector has been developed, featuring a finer pattern that allows fuel to also be introduced into the engine via the injector. The computing effort has been significantly reduced while maintaining the same resolution and the mixing of the fuel and oxidizer could be controlled more variably. This has opened up new possibilities for analysis. The flow field, combustion and performance paramters of this new engine variant is examined and compared to the initial injector design as well as to those drived from NASA CEA. To round off the performance scaling, the simulation results are compared with the test results from the De-Risk sub-scale engine. Before transitioning to the summary, conclusion, and outlook of this work, an important comment on the contour of the engine is made.

3.1 Mesh study

A crucial task in numerical flow simulation is to ensure that the results are not dependent by the computational mesh. A mesh that is too coarse leads to numerical errors and thus to deviations from physical reality. At the same time, a mesh that is too fine causes a considerable amount of computational effort. The goal of a mesh study is therefore to find the optimal balance: the mesh should be as fine as necessary, but as coarse as possible in order to save computing time. To ensure this independence from the mesh, a reference simulation with constant boundary conditions is performed on several meshes of varying fineness. The mesh resolution is increased step by step. If a mesh produces the same or nearly the same results as the next finer configuration, mesh independence has been achieved. The previous mesh can then be considered sufficiently fine and used for further simulations in the study. This mesh study examines the parameters of the prism layers, the fineness of the cells in the free stream of the combustion chamber, nozzle throat, and the expansion nozzle. The meshes used are listed in Table 3.1 with their configuration parameters. Initially, the focus was on resolving the boundary layer using prism layers. The starting point was a prism layer consisting of 25 layers with a growth factor of 1.2 from layer to layer and a thickness of the first layer of 0.01 mm. The 0.01 mm was chosen at random, while the growth factor of 1.2 was taken from the work of Hoffmann [1]. The value of 25 prism layers is based on experience from previous simulations.

Table 3.1: List of all used meshes used in the mesh study and their respective meshing parameters

variant	Global max. Cell Size	first layer thickness	Number of Layers	Max. cell size chamber & throat	cell size on injector openings
Mesh 1	3	0.01	25	3	1
Mesh 2	3	0.01	25	2	1
Mesh 3	3	0.01	25	1.5	1
Mesh 4	3	0.01	25	1	1
Mesh 5	3	0.01	25	1	0.1
Mesh 6	3	0.005	29	1	0.1
Mesh 7	2	0.01	25	1	0.1
Mesh 8	1	0.01	25	1	0.1

y^+-Value and thickness of the first prism layer

A y^+-value of one or less is necessary for good boundary layer resolution. In Ansys, it is possible to output y^+ values via contour plots. As is usual with other contour plots, the values are plotted on surfaces or cross-sections, and the individual gradients are indicated by color. What is striking about the y^+ contour plots of all meshes is that they express one color across the entire model and output practically only one value interval, regardless of where the sample is set on the surfaces. These values are listed for each mesh in Table 3.2.

Table 3.2: y^+-values of the used meshes. These values are taken from contour plots in Ansys Fluent.

variant	y^+-value	
	lower value	upper value
Mesh 1	1.019711	8.1734962
Mesh 2	1.163458	11.407336
Mesh 3	0.48242941	8.0717974
Mesh 4	1.2047317	8.013051
Mesh 5	0.4574379	3.5615065
Mesh 6	0.24294694	3.2703836
Mesh 7	0.44908395	2.9013999
Mesh 8	0.46197549	3.8369265

Looking at the lower value in each case, there are many values between 0.4 and 0.5. There are a few outliers with values just above 1. It is difficult to say where these outlier values come from, as they occur irregularly. No correlation with the number of iteration steps or mesh properties could be established. Assuming that the low y^+-value best reflects the actual y^+ at the surface for each mesh, it can be assumed that the thickness of the first layer, at 0.01, was already well chosen. In mesh 6, the thickness of the first prism layer was halved for testing purposes, resulting in a lower y^+ value of approximately half. Fluent therefore appears to be capable of establishing a correlation between the thickness of the first prism layer and y^+. However, reducing the first prism layer to below 0.01 mm is not necessary, as values below 1 are already obtained. As mentioned above, since the contour plots show no variation, as should be the case, it can be assumed that the y^+ values may not be determined as intended. This may be why the values are given at such large intervals for each point sample. Another indication of problems in determining y^+ would be the outlying lower y^+ values above 1, which cannot currently be explained. The values from Table 3.2 should therefore be used with caution. It is advisable to investigate the cause again for

subsequent work. For the rest of this paper, it is assumed that the thickness of the first prism layer is dimensioned correctly.
Another way to obtain y^+ values is to plot them on an xy graph. Figure 3.1 shows the y^+ value plotted over the CMC liner and the graphite tip. The injector plane is located at the left end, where several values are listed. These are difficult to explain, since it is assumed that there would be only one value. After that, the values along the inner CMC liner adopt the value zero and form a plateau. At the right end of the plateau, at the transition from the inner CMC liner to the graphite tip, there is then an abrupt increase to values between 8 and 10.3215. From there, the y^+ value decreases again until it approaches a value of 1.5. In the area of the injector plane and the graphite tip, the graph contains several y^+ values for each position. When reading the data file, 40 y^+ values were specified for one position, which is not physically plausible. One would assume either one value for each position or a maximum of two to indicate that the value lies within a range. In addition, the values are not linked in a row, but there are links across the graph. This raises doubts about the plausibility of the xy plots. The plot from Figure 3.1 comes from mesh 5, but this pattern also occurred in the simulations with all other meshes. The reason for all these discrepancies could not be determined. There was already a certain amount of skepticism regarding the y^+ values in Table 3.2. The output of the y^+ values via the xy plot raises even greater doubts, making the determination of the y^+ values via both variants even more questionable. In order to be able to continue with the mesh study, it is still assumed that the thickness of the first prism layer is sufficiently dimensioned, as already noted in Table 3.2, and the value of 0.01 mm is retained.

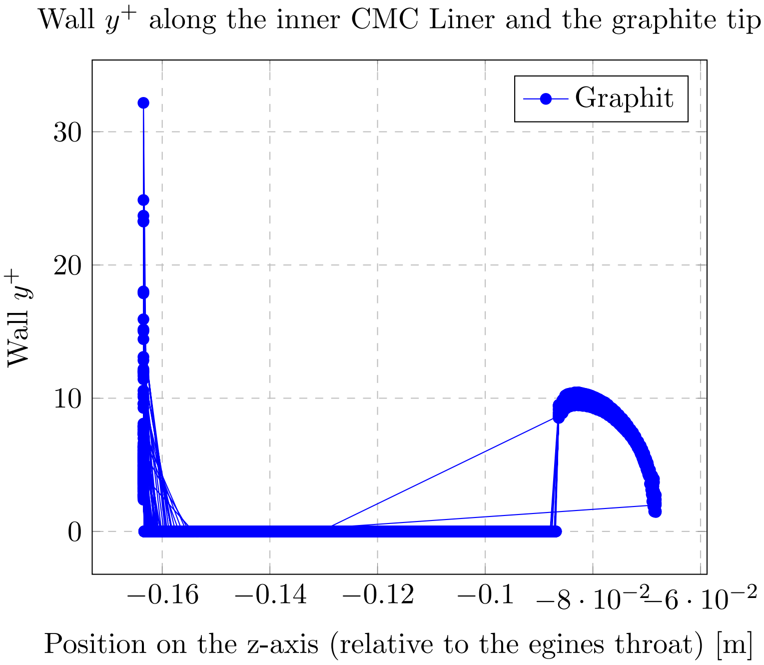

Figure 3.1: Wall y^+ distribution plotted over the inner CMC liner and the graphite tip of the engine. The injector plane is located on the left side. The abrupt increase in the values on the right side of the plateau marks the transition from the inner CMC liner to the graphite tip.

Height of the prism stack

Based on a thickness of the first prism layer of 0.01 mm, a growth factor of 1.2, and 25 layers, the theoretical stack height is 4.71981 mm. Considering that the combustion chamber gap at the injector level is only 6 mm wide, there is only room for one of the two prism layer stacks at this theoratical height. If both were placed fully developed in the combustion chamber gap, they would overlap. However, since both the prism layer stack of the outer and inner combustion chamber contours are implemented in the combustion chamber gap and Ansys Meshing inserts two layers of free cells to enable the transition between them, they both must have been compressed in order to fit into the available space. Assuming that Ansys Meshing continues to maintain the growth ratio of the cells at a level of 1.2 in this case, this means that in the respective prism layer stacks, each prism layer has been compressed or reduced in height—as has the first prism layer. This correlation can be seen in Figure 2.1. On the right-hand side is the sectional view through the combustion chamber gap, where the two prism layer stacks with two layers of free cells can be seen as a transition. In view of this, a thickness of 0.01 mm for the first prism layer may not be sufficient to obtain y^+-values of less than 1 in Table 3.2, but only through the compression of all prism layer cells due to the lack of space in the combustion chamber gap. The question of whether the prism layer stacks are sufficiently high to resolve the boundary layer is irrelevant, as there is no space at all to make the prism layer stacks any higher and have even been compressed in order to fit into the combustion chamber gap already.

Ratio of turbulent to dynamic viscosity

Since the ratio of turbulent to dynamic viscosity assumes low values in the laminar sublayer of the boundary layer and in free flow, and high values in the turbulent boundary layer, this ratio is suitable for determining the range in which the turbulent boundary layer is located. If this range is still within the prism layers, the boundary layer is located exclusively in this range and is dissolved by the prism layers. Figure 3.2 shows the viscosity ratio of two simulations in cross-section through the nozzle throat. On the left is the one from mesh 1, on the right is the one from mesh 5. In both cases, a streak with an increased viscosity ratio runs along the nozzle throat. In both cases, this is still within the range resolved by the prism layers. The shape of the plot from mesh 1 is also applicable to meshes 2, 3, and 4. The shape of the results in mesh 5 is almost identical for meshes 6, 7, and 8. For the area of the nozzle throat, the prism layers are therefore sufficiently dimensioned for all meshes.

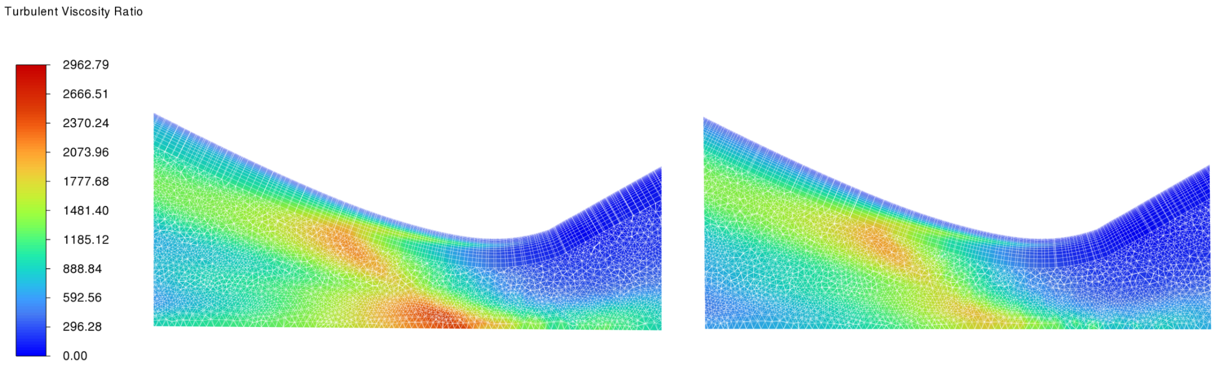

Figure 3.2: Viscosity ratio in the nozzle throat once in mesh 1 on the left and mesh 5 on the right.

Figure 3.3 shows the viscosity ratio for mesh 1 on the left and mesh 5 on the right in the cross-section through the combustion chamber. As expected, an area with an increased viscosity ratio would emerge within the upper and lower prism layers along the direction of flow, which would not extend beyond the transition from the prism layer cells to the tetrahedron cells of the free flow. However, in both meshes, an area with an increased viscosity ratio forms shortly after the injector, which extends almost over the entire height of the combustion chamber gap. In this unexpected case, the area extends beyond the transition from prism cells to tetrahedron cells. However, since it extends over the entire height of the combustion chamber gap, the question arises as to whether the cause is less due to insufficiently dimensioned prism layers and more due to the fact that the combustion chamber gap, with a height of only 6 mm at the injector level, favors local flow conditions in which an increased viscosity ratio occurs due to the limited space. For this reason the turbulent viscosity ratio is not considered as a reliable parameter when examining the combustion chamber gap. Here, too, the shape of mesh 1 is representative of meshes 2, 3, and 4, while mesh 5 is representative of meshes 6, 7, and 8.

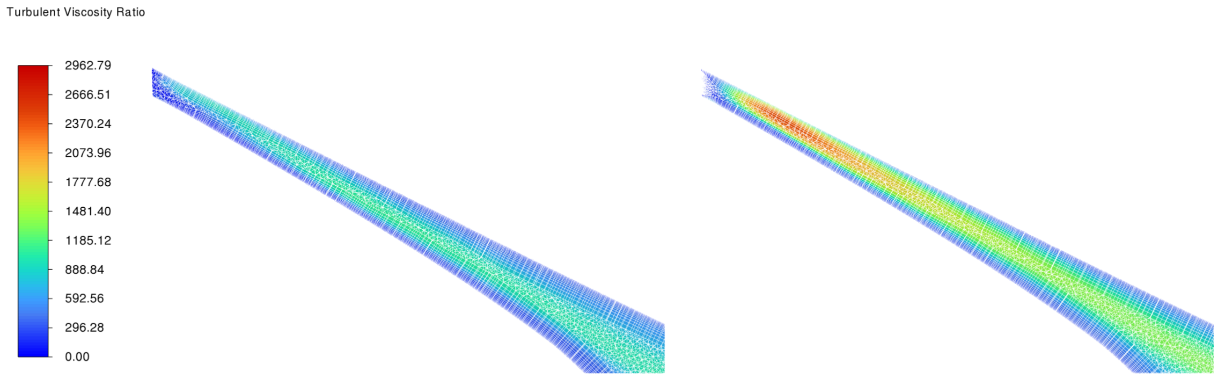

Figure 3.3: Viscosity ratio in the combustion chamber gap once in mesh 1 on the left and mesh 5 on the right.

Free cells

After extensive consideration of the resolution of the boundary layers, the influence of the free cells on the flow will now be examined. The combustion chamber pressure of the mesh variants will be considered as a reference point. For illustration purposes, this is plotted over the mesh variants in Figure 3.4. From mesh 1 to mesh 4, only the fineness of the cells in the combustion chamber and the nozzle throat is increased. When looking at these four points, there is no apparent dependence of the combustion chamber pressure on the fineness of the free cells. This is mainly due to the pressure of mesh 1, which is clearly higher than the pressure of the next two finer meshes. Since there is an asymptotic behavior in combustion chamber pressure as a function of the number of cells from mesh 2 to mesh 8, mesh 1 appears to be an outlier. Mesh 6 is also striking, as it has a slightly lower pressure than mesh 5. However, in this case, the change is due to the refinement of the boundary layer and not to the free flow. Due to the small number of measurement points, it is difficult to substantiate the statements on the mesh variants. A more detailed examination of several mesh variants and varying reference simulations could provide more insight here. The heat flows through the walls were used for further evaluation of the mesh variants. In chapter 2.1, it was already mentioned that temperatures were assigned to the walls of the engine so that heat flows through the walls could be determined. Depending on how the heat

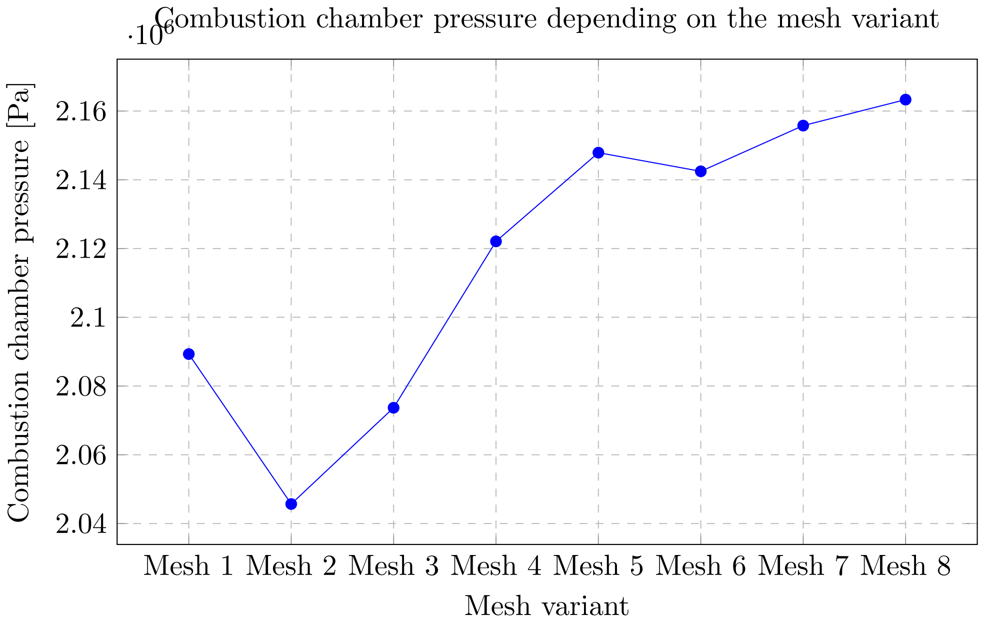

Figure 3.4: Comparison of the pressure between different simulation variants.

flows develop from mesh to mesh, there could be a correlation between the fineness of the mesh and the accuracy of the numerical solution. The evaluation of the heat flows in the simulations did not reveal any clear patterns, and the values changed significantly when the calculations were repeated. It has been found that the values of the heat flows, especially through the wall of the expansion nozzle, fluctuate greatly from iteration to iteration within the simulations. This explains the change in patterns when the heat flows are plotted on graphs. The heat flows are therefore difficult to compare with each other and are therefore not used to evaluate the meshes. However, it should be noted that there is a problem with the reliable development of the heat flows and that there may be a problem that also affects the accuracy of other parameters in the simulation.

Conclusion

Since meshes 1, 2, and 4 were already conspicuously high in Table 3.2 with their lower y^+-values of over one, and mesh 1 also showed an inexplicably high pressure in Graph 3.4, these meshes are considered as unsuitable. This leaves meshes 5, 6, 7, and 8. After careful consideration of Table 3.2, the thickness of the first prism layer in mesh 6 is finer than necessary, and mesh 5 is preferred over mesh 6. However, in order to keep the computational effort of the simulations low, mesh 5 is selected for further consideration as the variant with the lowest number of elements among the remaining meshes.

3.2 Pressure boundary

As already mentioned in Chapter 2.1.3, the pressure boundary condition not only has a significant influence on the convergence behavior of the simulation, but also on the flow pattern within the expansion nozzle, provided that it is higher than the pressure that naturally occurs in the flow at the exit. For this reason, the influence of the pressure boundary condition at the exit was investigated by numerical experimentation. Since the engine is an upper-stage engine and it is practically in a vacuum during operation, the simulations were initially initiated at low pressures. These were, then, gradually increased depending on the results.

Coarse mesh

Initially, the investigations were conducted early in the work for this thesis, when significantly coarser meshes were still used for calculations. These investigations where then repeated later when the final meshes were available. The first table (Table 3.3) lists the influence of various pressure boundary conditions based on an old mesh, which has a free flow fineness in the expansion nozzle of 5 mm and a boundary layer resolution of 7 elements with a maximum thickness of 6 mm and a growth rate of 1.2.

Table 3.3: Varying pressure exit boundary conditions and their effect on the convergence and simulation results on an old mesh

0 Pa	Failed to initialize
1 Pa	crashed after 16 iterations
10 Pa	crashed after 9 iterations
100 Pa	crashed after 65 iterations
1000 Pa	fully developed flow stream
101325 Pa	flow separation in expansion nozzle

All simulations crashed at pressures up to 100 Pa, and Fluent was unable to initialize the calculation at an ambient pressure of 0 Pa. At a value of 1000 Pa, the simulation then runs stably and the flow develops as expected, similar to Figure 3.7. In this case, a pressure between 2260 Pa and 4350 Pa is established in the simulation at the exit plane. Consequently, this boundary pressure level (1000 Pa) provides a basis for initiating the solution, and the actual solution is established over the course of the calculation. The lower limit of the pressure at the outlet level is established by itself and is not enforced by the boundary condition. Here, it was interesting to observe the results when the pressure boundary condition is set to a value above the naturally occurring pressures. To do this, the pressure was set to atmospheric pressure (101325 Pa), creating the conditions of a ground-level test. The flow cannot develop fully, resulting in separation in the expansion nozzle. Figure 3.5 shows the temperature profile of the flow in a longitudinal section through the engine. The flow proceeds as expected in the combustion chamber and nozzle throat and separates in the expansion nozzle. Fluid from the environment flows upstream along the walls of the expansion nozzle. From the point at which the flow of the engine has the pressure of the returning outside air, the outside air is deflected toward the center of the engine and flows along with it. As expected, the combustion chamber pressures of the two simulations proved to be identical. In the simulation with a pressure boundary condition of 1000 Pa, the combustion chamber pressure ranged from 2204196.8 Pa to 2226438.5 Pa. In the simulation with a pressure boundary condition of 101325 Pa, the pressure ranged from 2205930.3 Pa to 2228143.5 Pa. This corresponds to a deviation of 0.09% between the two combustion chamber pressures. This is due to the fact that the information from the two flow patterns is unable to pass through the nozzle throat, as supersonic flow occurs there, resulting in the same conditions in both combustion chambers.

Current mesh

The value of 1000 Pa for the pressure boundary condition at the engine outlet was used for the following calculations. However, during the mesh study, it was noticed that the pressure at the

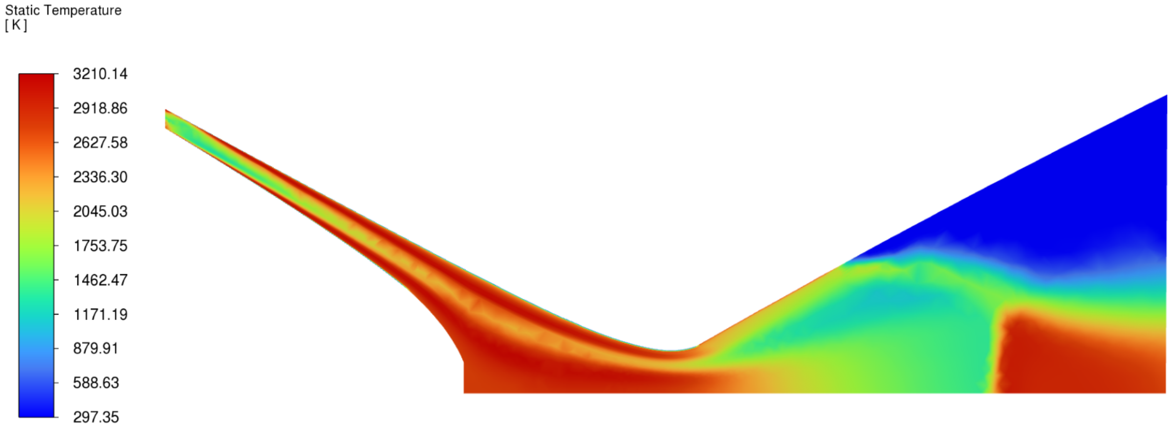

Figure 3.5: Sectional view of the temperature profile of the flow in the engine at a pressure boundary condition of 101325 Pa.

end of the expansion nozzle no longer had a value of 2260 Pa and 24503 Pa, but instead settled at 1000 Pa. The use of finer meshes must have a numerical effect on the calculation such that lower pressures are established at the end of the expansion nozzle. The effect of the fineness of the mesh on the established pressure at the end of the expansion nozzle and on the stability behavior of the calculations as a function of the selected pressure at the boundary condition is to be checked using mesh 5. Calculations were performed with successively increasing pressures at the outlet pressure boundary condition and their influence was documented. The results are listed in Table 3.4. As expected, Ansys Fluent, similar to the old mesh, has difficulty initiating the solution at 0 Pa and crashes after only a few iterations at values from 1 Pa to 200 Pa. The pressure was then increased to 500 Pa. Here, the simulation was able to stabilize after 270 iterations, and pressures of 500 Pa to 22396 Pa were established in the exit plane. It is noticeable here that the calculation does not run stably at the beginning, which may mean that the pressure is almost set too low but still the results seem to settle aftificially at a minumum pressure of 500 Pa. This suggests that even lower pressures can occur if the pressure boundary condition is set lower. Therefore, a new calculation was performed with a pressure boundary condition of 300 Pa. This stabilized after 1000 iterations. An interval of 300 Pa to 22215 Pa was output over the area of the exit plane. It is interesting to note that the pressure boundary condition again represents the lower limit of the resulting pressures. This raises the question again as to whether even lower pressures would occur if the pressure boundary condition were lowered below 300 Pa. The only question is how far this is possible, as the simulation crashes at a pressure of 200 Pa. When the upper limit of the pressure output range is reduced from up to 22 bar combustion chamber pressure to 10,000 Pa, the pressure output at the exit plane is more specified. Instead of indicating the pressure across

Table 3.4: Varying pressure exit boundary conditions and their effect on the convergence and simulation results on mesh 5.

0 Pa	Failed to initialize
1 Pa	crashed after 9 iterations
10 Pa	crashed after 23 iterations
100 Pa	crashed after 83 Iterations
200 Pa	crashed after 74 iterations
300 Pa	stabilized after 1000 iterations
500 Pa	stabilized after 270 iterations

the exit plane in a single color and with the relatively large intervals used previously, the pressure at the exit plane is now represented with a fine color gradient and the pressures are now indicated in narrower intervals in point samples. This shows that Ansys Fluent reduces the resolution of small gradients when the global range of values is significantly higher. Now the pressure at the center of the exit plane lies between 2000 and 2100 Pa and rises to 4100 to 4200 Pa towards the edge. If the upper value of the pressure output for the old mesh is also set to 10,000 Pa, pressure values between 2260 and 2338 Pa are obtained in the center of the exit plane and between 4273 and 4350 Pa in the edge area. So, the pressure values along the exit plane are similar for the old mesh and mesh 5, with the values for mesh 5 being slightly lower. But where do the values of 300 Pa occur? They can be found at mesh 5 at the outermost edge, where the boundary layer of the expansion nozzle wall is located. In the old mesh, however, no boundary layer coming from the expansion nozzle can be seen at the edge of the exit plane. This may be because the boundary layer is better resolved in mesh 5. In summary, Ansys Fluent requires a certain pressure level at the pressure outlet condition for initialization and for a stable calculation, even if the real environment is a vacuum. If the pressure level exceeds the naturally occurring pressures, the minimum pressures at the exit plane are maintained artificially at this level. This results in higher pressures than would actually occur. Especially low pressures are to be found in the boundary layer. It is important for future simulations to be familiar with the environmental conditions, as well as the meshing and boundary layers, to ensure the accuracy of the results. Another advice is to initiate simulations at higher exit pressures in the future and to lower the pressure as soon as the simulation has stabilized. If the pressure boundary condition is set high in accordance with an environmental condition, physically meaningful results are obtained, such as the separation of the flow in the expansion nozzle at sea level.

3.3 Flow pattern

Now, an overview of the flow pattern of the engine will be given. The pressure and temperature will be addressed for the entire engine before examining each area individually.

Pressure

A pressure of approximately 2147932.3 Pa, i.e., 21.47 bar, is established in the combustion chamber. This means that the pressure is 1.47 bar above the pressure of 20 bar specified in the design in 1.3. At the end of the combustion chamber, the pressure is reduced to about half at the nozzle throat, which is physically sensible and is a general rule of thumb for engines [14]. The pressure continues to decrease towards the end of the expansion nozzle. As already mentioned in the previous chapter, pressures of 2000 Pa prevail in the core of the flow and 4400 Pa at the edge of the expansion nozzle in the exit plane. Figure 3.6 shows the pressure curve in the sectional view.

Temperature

The temperature curve provides significantly more information about the flow pattern of the engine (see Figure 3.7). In the combustion chamber, the combustion processes of the engine are clearly visible in the red areas. From the injector, the oxidizer extends as a lower temperature area along the entire combustion chamber. It is noticeable that shortly after entering the injector, this area adheres to the contour of the inner hyperboloid—more on this in the following section. Gradually, combustion zones form in the combustion chamber and the oxidizer streak slowly

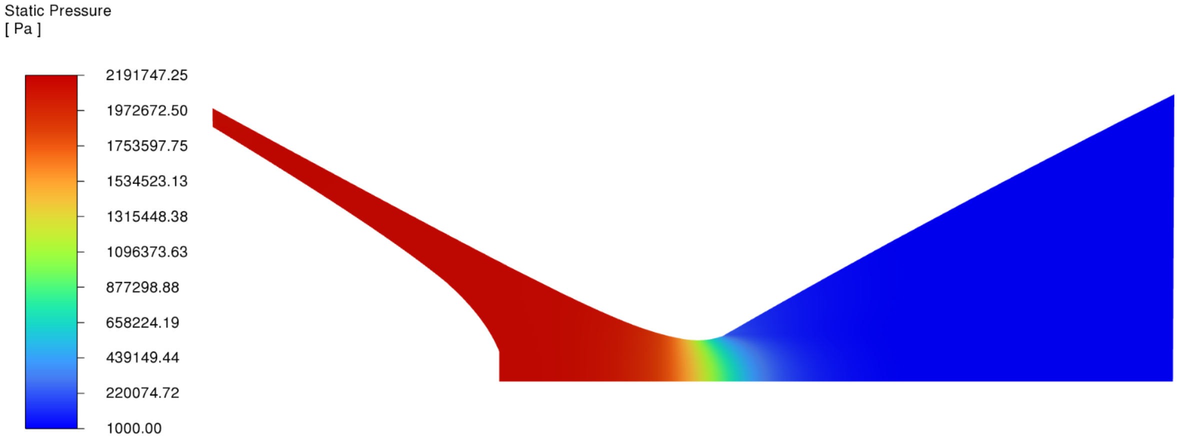

Figure 3.6: Pressure profile of the engine in the sectional view

becomes narrower and less pronounced. However, the oxidizer streak is not completely consumed before the end of the combustion chamber. At the tip of the inner hyperboloid, there is an area of lower temperature. This will be examined in more detail in the following sections. It can be assumed that unburned fuel collects here from the boundary layer and remains in a kind of wake of the inner hyperboloid. It can also be assumed that vortices occur in this area. In the nozzle throat, starting from the outer contour towards the center of the flow, there is a colder boundary layer, a mixing and combustion zone originating from the outer contour, the still present temperature signature of the oxidizer streak, the area of mixing and combustion originating from the inner contour, and a cooler streak originating in the flow-calmed area at the end of the inner hyperboloid. In the expansion nozzle, this flow pattern changes only insofar as the areas continue to expand in the radial direction and their temperatures decrease. Particularly striking is how pronounced the differences in temperature ranges are to the eye. It can, therefore, already be said at this point that the flow in the combustion chamber is not homogenized, which means efficiency losses and, therefore, performance impairments to the engine.

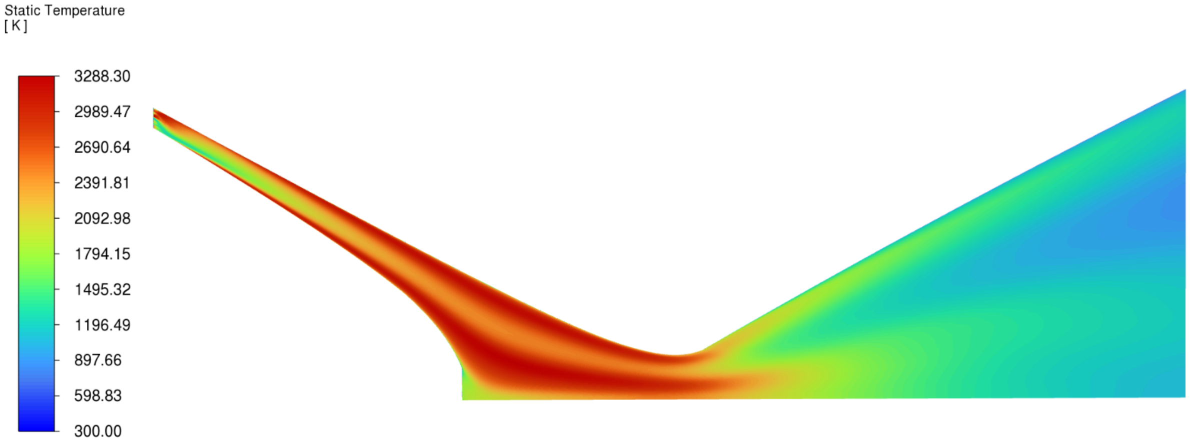

Figure 3.7: Temperature profile of the engine in the sectional view

Injector region

When looking at the temperature curve, it is already apparent that the flow near the injector initially follows the contour of the inner hyperboloid. A look at the vector field in this area should provide some insight. It is displayed in Figure 3.8 in a cross-section through the engine. The plot is taken from a plane where there are three injector openings at the beginning of the combustion chamber, which can be recognized by the areas with high density of vectors. As expected, the arrows show that the flow from the injector slots drops and adheres to the liner surface. In the area above the adjacent flow, a vortex is created, on the upper side of which the flow even flows toward the injector. The fuel appears to be carried away from the outer contour toward the injector and mixed into the oxidizer flow there. This means that there is no homogeneous outflow toward the nozzle throat and the oxidizer flow comes into direct contact with the liner surface. This is particularly unfavorable because the oxidizer oxidizes the CMC liner and thus “burns” it away. Black Engine Aerospace GmbH has an inner hyperboloid on display that was used to conduct engine tests on another similar engine, and it shows elongated grooves in the wake of the injector slots. Figure 3.9 shows a picture taken from said inner hyperboloid. These originate from the fact that the CMC liner is being burned in these areas. The fact that these areas are located directly in the wake of the injector slots suggests that the burning is particularly related to the oxidizer and that the oxidizer flow in this engine also adheres to the contour of the inner hyperboloid in the wake of the injector. A look at the pathlines in Figure 3.10 provides further insight. There, the pathlines of several particles originating from the injector slots are shown on a 30° section of the injector. It can be seen that the flow from the injector slots along the entire injector drops to the contour of the inner hyperboloid. This may be a phenomenon typical of the dual-shell hyperboloid and needs further investigation. In any case, remedial action must be taken when this occurs, as it shortens the service life of the engine or even damages it. It has been, therefore, decided to manufacture the CMC Liners out of oxide ceramics in the future as they are resistant to oxidation. This might resolve the issue but it has to be proven in upcoming engine tests first.

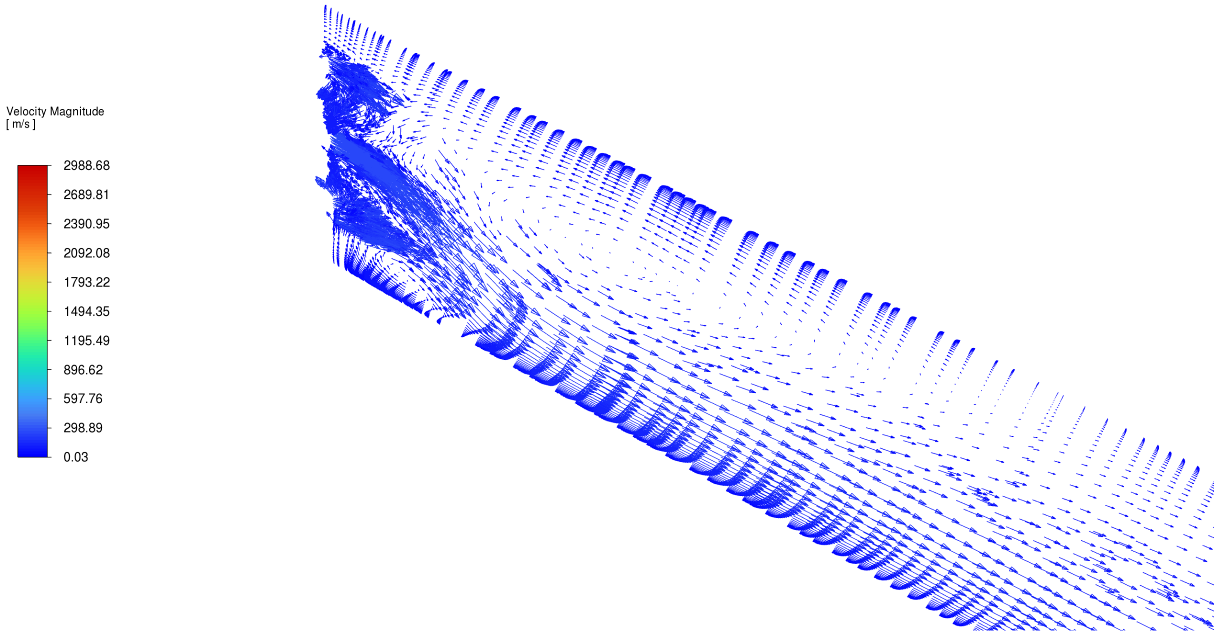

Figure 3.8: Vector field in the vincinity of the injector.

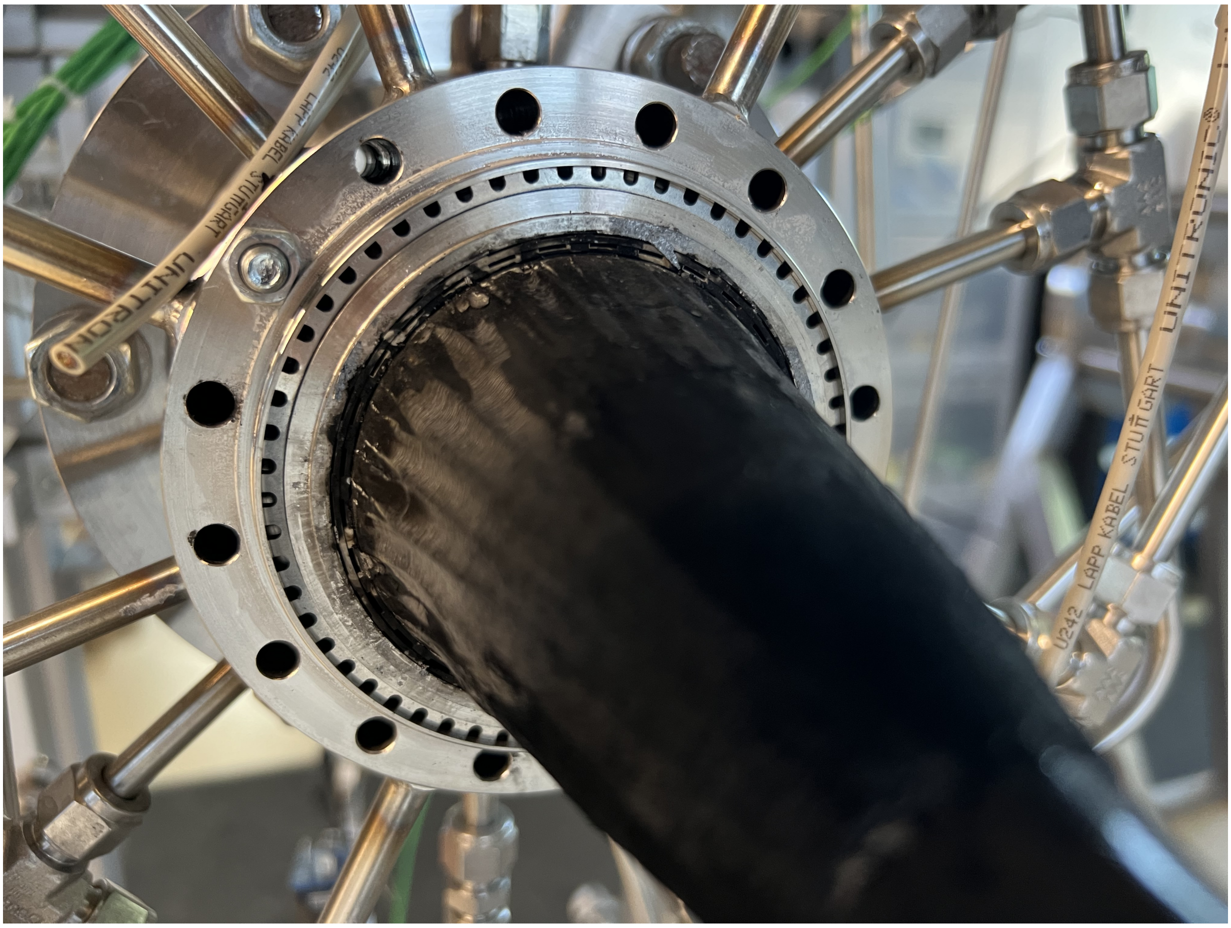

Figure 3.9: Image of an internal hyperboloid that was subjected to engine tests on a test stand at the BEA site. The inner hyperboloid can be seen because the housing and the outer hyperboloid of the engine were dismantled. On the inner hyperboloid, furrows can be seen in the wake of the injector openings, which indicate that the CMC liner has come into contact with the oxidizer and has therefore been oxidized. The Liners are manufactured out of C/C (Carbon/Carbon). As a highly sensitive surface material it is predominantly used to indicate and identify surface effects.

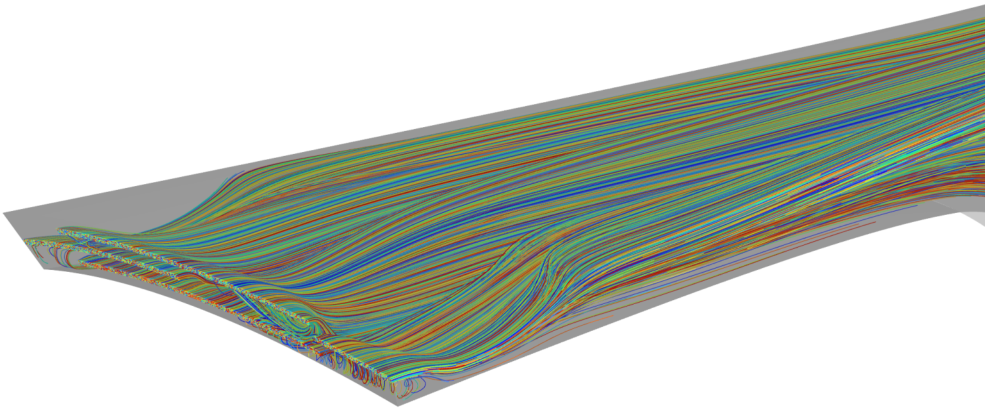

Figure 3.10: Pathlines of the injector inlets in the vicinity of the injector. The walls of the computing domain are depicted in a transarent gray tone.

Another aspect of the flow pattern is that the injector has a non-symmetrical slot pattern. The pattern of the engine consists of opening slots oriented in the circumferential direction. The number of slots in the circumferential direction periodically changes from one slot to two to three before repeating from three slots back to one, as already shown in Figure 1.6. This periodicity may result in flow components in the circumferential direction, which might cause efficiency losses in the engine. The flow pattern is to be examined for components in the circumferential direction in order to identify possible phenomena depending on the injector pattern. Figure 3.11 shows the pathlines starting from a longitudinal section through the engine. In the vicinity of the injector, clear deviations of pathlines from the longitudinal plane in the circumferential direction can be seen. It is particularly important that the predominant direction at the start of the path lines points in the circumferential direction. It can therefore be assumed that the periodic injector pattern encourages flow components in the circumferential direction, which might cause efficiency losses.

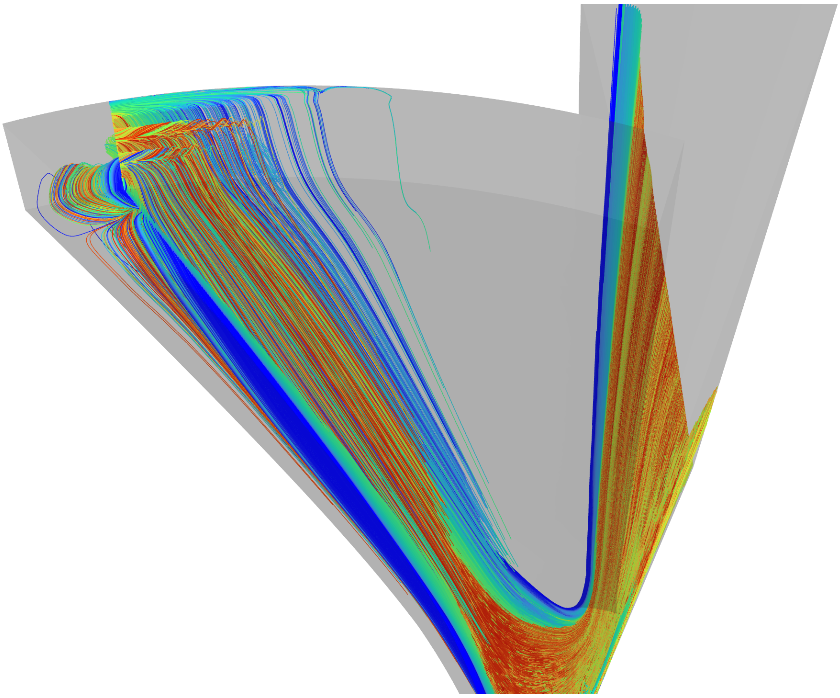

Figure 3.11: Pathlines originating from the longitudinal plane. The walls of the computing domain are depicted in a transparent gray tone. The combustion chamber is in the foreground, the expansion nozzle in the background.

Combustion chamber

Further into the combustion chamber, the vortex field then homogenizes and all arrows point in the direction of the expansion nozzle, as can be seen in Figure 3.12. One thing is particularly striking here: the arrows on the upper and lower contours also run in the direction of flow toward the nozzle throat. In transpiration cooling, the idea is that the boundary layer is blown off. Accordingly, one would expect that the arrows on the contours would have at least one component perpendicular to the liner surface, but this is not the case. They run parallel to the surface of the liners. This raises the question of whether the modeling has reached its limits here, or whether transpiration cooling is not capable of blowing off the boundary layer.

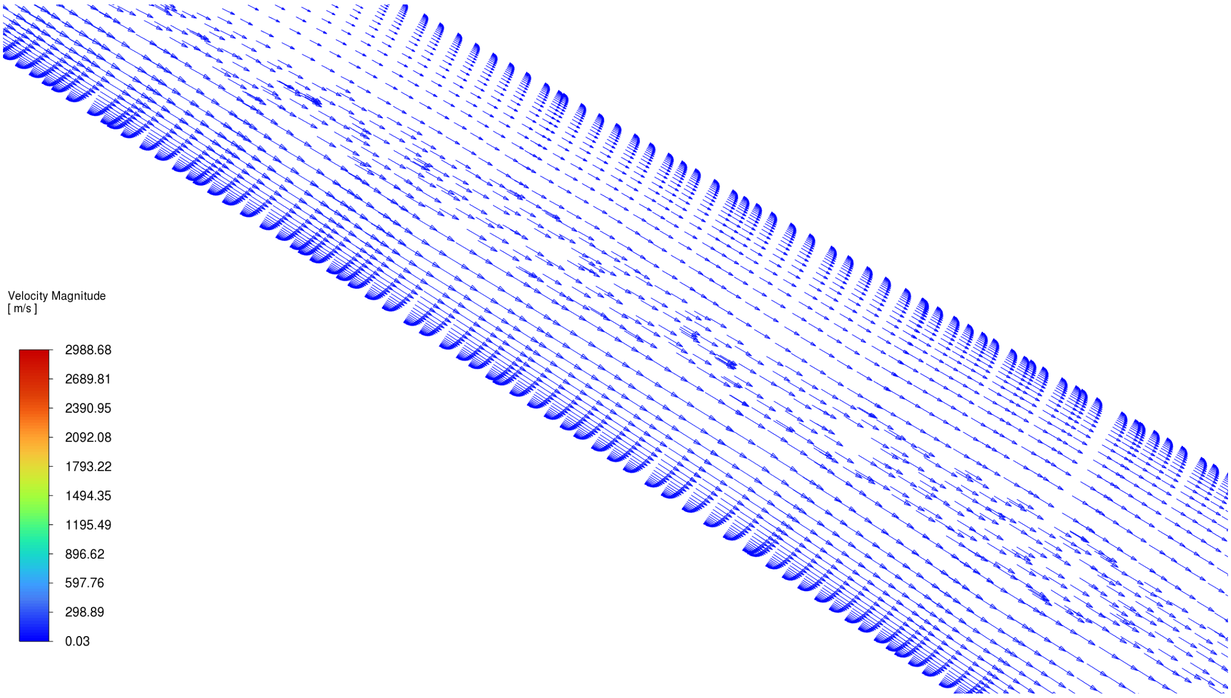

Figure 3.12: Vector field in the combustion chamber shown in longitudinal section

End of the inner hyperboloid

At the end of the inner hyperboloid, the flow near the wall in Figure 3.13 tends to run parallel to the wall surface, while the free flow is increasingly deflected toward the nozzle throat. The tip of the inner hyperboloid is slightly cut off. The discontinuous transition causes the boundary layer to separate there, which then also deflects toward the nozzle throat. A vortex forms in the quasi-cut-off volume of the hyperboloid. In the temperature curve of the engine (Fig. 3.7), this is noticeable at the end of the inner hyperboloid as an area of low temperature. Due to the low temperature, it can be assumed that there is unburned fuel in the vortex. The temperature curve also showed that a fine, cold stream bleeds off from the vortex and extends through the nozzle throat into the expansion nozzle and finally into the environment. This is reflected in the vector field by the fact that the vortex splits at the symmetry line of the engine and part of it flows off in the direction of the nozzle throat. Originally, a small injector for the oxidizer was planned at the end of the inner hyperboloid. Its absence makes it apparent that at least a small amount of unburned fuel flows along this area. It is therefore quite conceivable that implementing the originally planned injector with a small oxidizer flow could potentially improve the completeness of the combustion.

Throat

The resulting flow regions in the throat have already been covered in the observation of the temperature profile. The only remaining aspect is to verify a successul Mach transition in the throat. Figure 3.14 is therefore consulted and it indeed reveals a Mach transition.

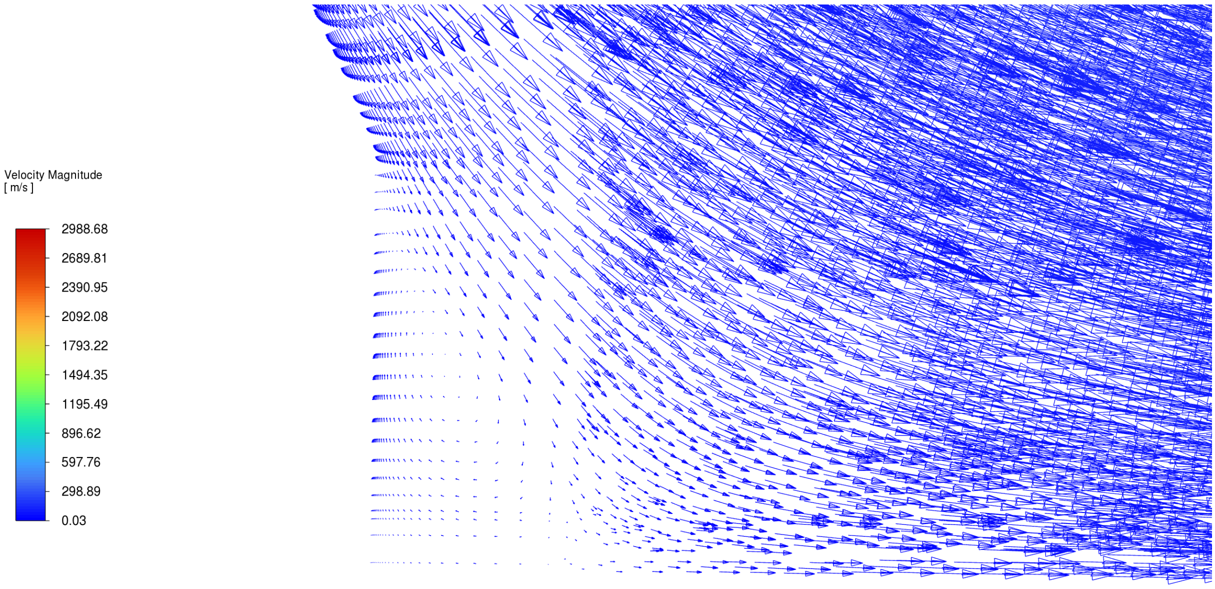

Figure 3.13: Vector field at the end of the inner hyperboloid shown in longitudinal section

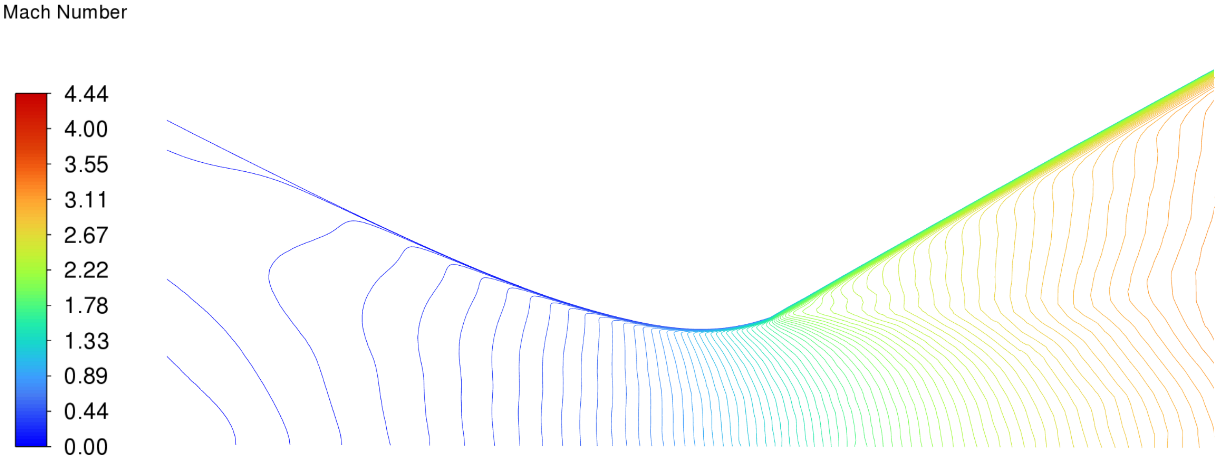

Figure 3.14: Ma-distribution in the engines throat

Expansion nozzle

The development of different areas from the throat into the expansion nozzle has already been explained in the discussion of temperature. In Figure 3.15 the vector field of the expansion nozzle is displayed. It shows that flow does indeed expand into the whole expansion nozzle and not detach at any point. The stream of unburned oxygen is easy to discern in the temperature curve in Fig. 3.7. However, in the vector field this is more difficult as the arrows are colored based on their velocity and based on this coloring the streak of oxygen appears to have an only slightly lower velocity than its surrounding flow.

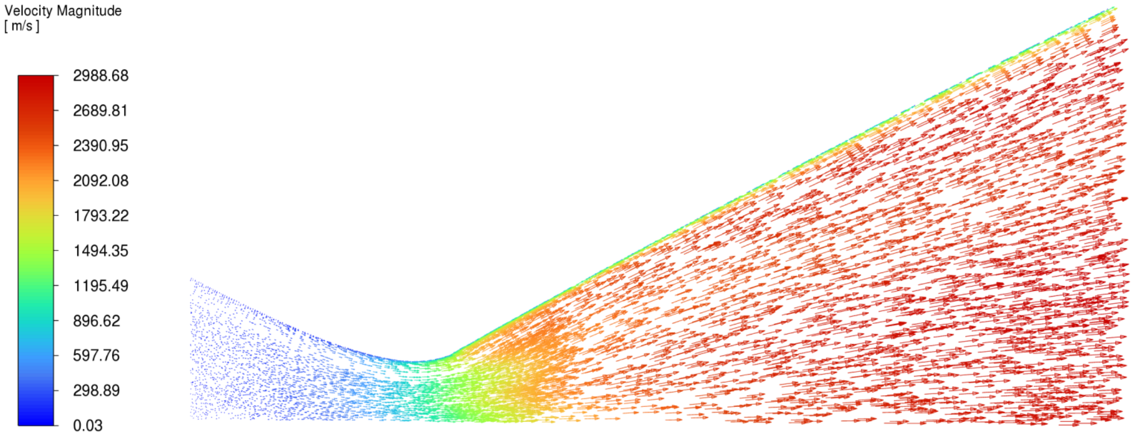

Figure 3.15: Vector field of the expansion nozzle of the engine

3.4 Implementation of the transpiration cooling

Three possible approaches to implementing transpiration cooling were tested. The first was to set a mass flow boundary condition at the surfaces of the CMC liner. This variant is particularly attractive because it is easy to implement and the desired mass flow is set as a fixed condition in Ansys Fluent. The inlets on the CMC liners were also defined as velocity boundary conditions. In this case, as with the mass flow inlet, the pressure, temperature, and composition of the inflowing fluid are specified in Fluent. The difference is that an inflow velocity is set as a fixed condition and the mass flow is calculated during the simulation from this velocity, the set density, and the flow area of the boundary condition. Since mass flows are fundamental parameters in the design, operation, and classification of rocket propulsion systems, the mass flow boundary condition has a clear advantage over the velocity boundary condition in that the mass flows can be specified from the setup and do not have to be determined over the course of the simulation. In order to obtain the appropriate mass flow using the velocity inlets, iterative simulations had to be performed and the inflow velocities of the fuel had to be adjusted at every iteration. An interesting observation was that once the appropriate values for the velocities had been found in a simulation with one mesh, they could also be used for another mesh. This was even possible between two meshes that differed not only in the fineness of the meshing, but also in the fact that one mesh was a 4.28° section of the engine and the other was a 30° section.

Table 3.5 lists the necessary input values for the mass flow and velocity boundary conditions for the inner and outer liners. While the values for the velocity inlet had to be determined interactively and can be applied to other meshes regardless of the width of the periodic section from the engine, the mass flow rate for the mass flow inlets is known from the setup, but the values must always be adjusted when the width of the section from the engine changes. Therefore, when specifying the mass flow inlet parameters in Table 3.5, it should be noted that the values are the mass flows for an engine section of 30°.

Table 3.5: List of the inlet parameters for the mass-flow inlet and the velocity-inlet

Inlet	Inlet mass flow [kg/s] (30° section)	Inlet velocity [m/s]
Outer Liner	0.005247	0.020286
Inner Liner	0.003253	0.021134

The two variants were to be compared here using a reference simulation on mesh 5, but it was not possible to set up a stable simulation with velocity inlets for transpiration cooling on mesh 5. This was surprising, as there is already a stable calculation on a comparable mesh, which is also a 30° section and with 809,692 elements has a similar number of elements to mesh 5. To enable a comparison, the comparative simulations were performed on this mesh. As expected, the mass flow simulation yielded the exact kerosene mass flows through the inner and outer liners as specified in Table 3.5. Using the values set in this table, the simulation with the velocity inlets at the CMC liners resulted in mass flows of 0.00525 kg/s through the outer liner and 0.00326 kg/s through the inner liner. This corresponds to a deviation of the mass flows from the ideal value through the velocity inlet of 0.057% at the outer liner and 0.215% at the inner liner. With such a small deviation, the simulations can be considered similar enough to be compared in terms of their flow pattern. The contour plots of the temperatures in Figures 3.16 and 3.17 show no discernible qualitative differences in the flow.

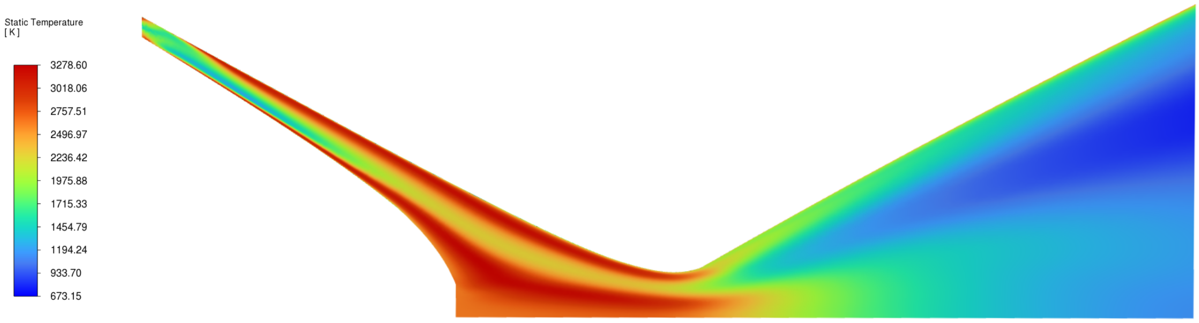

Figure 3.16: Contour plot of the static temperature for the velocity inlet

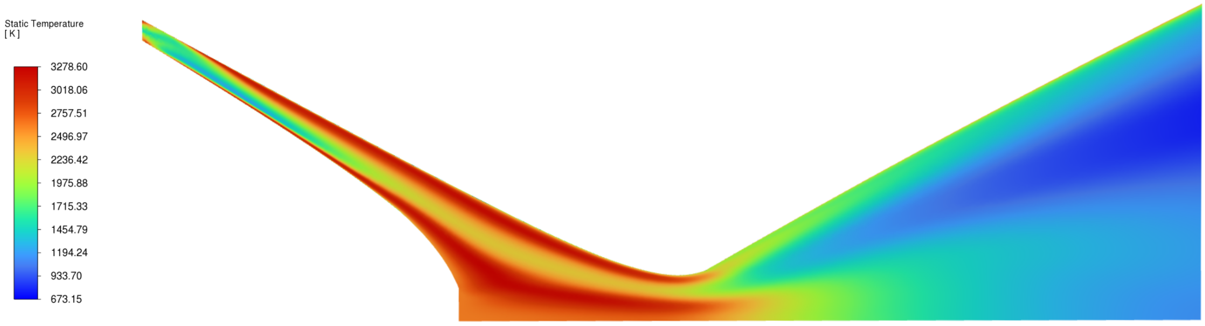

Figure 3.17: Contour plot of the static temperature for mass-flow inlet

In terms of combustion chamber pressure, Table 3.6 also shows a deviation of only 0.3% in combustion chamber pressure. Here, too, the differences are minor.

Table 3.6: Resulting Pressures between mass-flow inlet and velocity inlet

Inlet	Pressure [Pa]
Mass-flow inlet	2129718.5
Velocity inlet	2136303.3

With regard to the blowing off of the boundary layer, which was already mentioned in Chapters 2.1.5 and 3.3 and is a desired effect of transpiration cooling, there appears to be no difference in the representation using the vector fields in the combustion chamber. In Figure 3.18, these are shown side by side for the velocity inlet and the mass flow inlet. Unfortunately, it can be seen that in both variants, the vectors on the linear surfaces do not have any components perpendicular to the surface, but instead flow parallel to the surface.

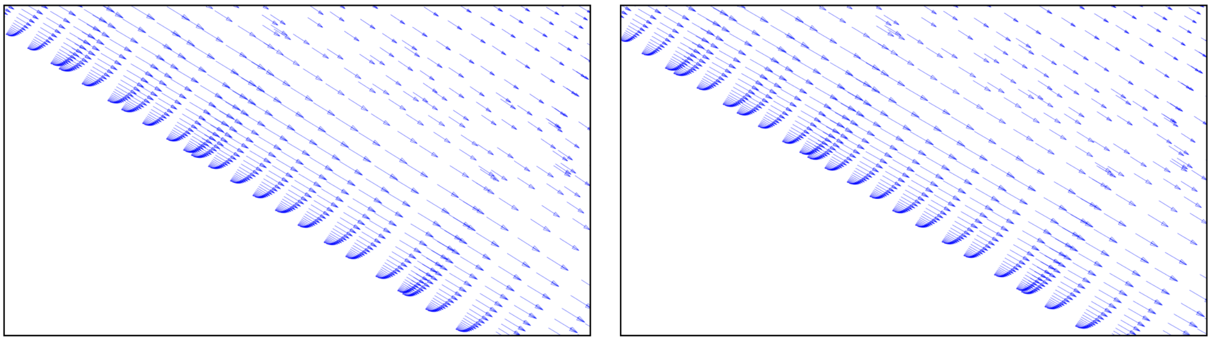

Figure 3.18: Comparison of the vector fields of the two inlet variants. The vector field of the transpiration cooling implemented via mass-flow inlet on the left and via velocity inlet on the right

It seems like there is little to no difference between these two variants. The only markable difference could be found when looking at the thrust and specific impulse that these two variants yield. They are listed in Table 3.7. Apparently the mass flow-inlet yields a 4.8% higher thrust and specific impulse than the velocity inlet variant.

Table 3.7: Resulting thrust and spceific impulse between mass-flow inlet and velocity inlet

Inlet	Thrust [N]	Specific impulse [s]
Mass-flow inlet	2883,74	293,96
Velocity inlet	2750,78	280,41

So, in the end, there is little to no difference between the two variants in terms of the results that they produce. Moreover, the one difference in thrust of 4.8% does not tell if either of those approaches is more physically accurate. The main driver to choose the implementation of the transpiration cooling via the mass-flow inlet over the velocity inlet remains the fact that the mass flow inlet is more practical in use, since it sets the mass flow as a hard condition which leads to exact mass flows in every calculation, while the velocity inlet requires iterative setting of the input parameters, until the right mass flow is found. For tests on the engine, however, the velocity value from the velocity inlet at which the fuel enters the combustion chamber is used to calculate the pressure at which the fuel should be pressed into the CMC liners on the cold gas side. The Darcy-Forchheimer equation [15] is used for this purpose:

$$\frac{P_i^2 - P_o^2}{2PL} = \frac{\mu}{k_d} v_s + \frac{\rho}{k_f} v_s \tag{3.1}$$

Here, P_i is the pressure on the cold gas side, P_o is the pressure in the combustion chamber, P is the pressure at the point of observation, L is the sample thickness, μ and ρ are the viscosity and density of the fluid, v_s is the volumetric fluid velocity, and k_d and k_f are the Darcy and Forchheimer coefficients. The k_d and k_f values were determined experimentally at DLR and amount to $k_d = 2.01 * 10^{-13}\ m^2$ and $k_f = 4.98 * 10^{-8}\ m$. Since the velocity values (Table 3.5) have been determined at the combustion chamber side of the CMC liners, all parameters are set to represent this environment. P is set to be equal to P_o (combustion chamber pressure) which is 2136303 Pa. The sample thickness in the varies alonog the combustion chamber between 6.77 mm and 10.03 mm. So for L an average value of 8.5 mm has been set. With $\mu_v ap = 20.95 * 10^{-}6kg/ms$ and $\rho_v ap = 131.348kg/m^3$ and a velocitiy taken from the inner liner in Table 3.5 of $v_s = 0.0211335m/s$ the Darcy-Forchheimer equation yields a pressure of 2164850 Pa on the cold gas side of the CMC Liner. This value will be targeted in upcoming engine tests to check whether transpiration cooling develops as expected. For the further course of the study, it is noted that there were no major differences between the two approaches to implementing transpiration cooling, either via mass flow inlet or velocity inlet, and that the mass flow inlet continues to be preferred due to its practical applicability.

One disadvantage of mass-flow and velocity inlets is that Ansys Fluent distributes the resulting flow homogeneously across the entire liner surface. In reality, however, a certain degree of unevenness would occur. This is due to the fact that the wall thickness of the CMC liner is not constant in the direction of flow, which means that the cooling medium encounters resistance that varies in the direction of flow when entering and passing through the porous liner. The second factor that affects the uniformity of the inflow across the entire liner surface is that the fuel is not supplied evenly to the rear of the liner.

As a supplement to the mass-flow inlet and the velocity inlet, a third variant for modeling transpiration cooling was tested. The idea was to additionally model the CMC liners as porous domains in Fluent and to apply the fuel to the liners from the outside using a pressure boundary condition. The kerosene would flow through the liners into the combustion chamber. This would make the simulation more realistic. On the one hand, the varying wall thickness of the CMC liners would be taken into account, which would result in a realistic representation of the distribution of the kerosene inflow through the liner surface. On the other hand, the surface roughness of the CMC liner can be modeled. Another advantage is that the heat flows through the liner surface can be modeled. A suitable model for this variant has been created. Figure 3.19 shows a model that includes the inner chamber of the engine as well as the outer and inner CMC liners as porous domains. This is a particularly narrow section of the engine in order to save computing time. The domains are connected to each other at their contact surfaces by means of interfaces. Pressure boundary conditions are set on the inner side of the inner liner and on the outer side of the outer liner, through which the kerosene is introduced into the liners. These are marked by blue arrows. Like the section of the engine, the porous domains have periodic boundary conditions at their cut surfaces. Unfortunately, the simulations with this model crashed after only a few iterations. The cause could not be identified. The residues of the energy equation were already 10^{35} at the start of the simulations and diverged further from there. Future studies might investigate this approach further in order to eventually obtain a model that runs stably so that further insights to the transpiration cooling can be obtained.

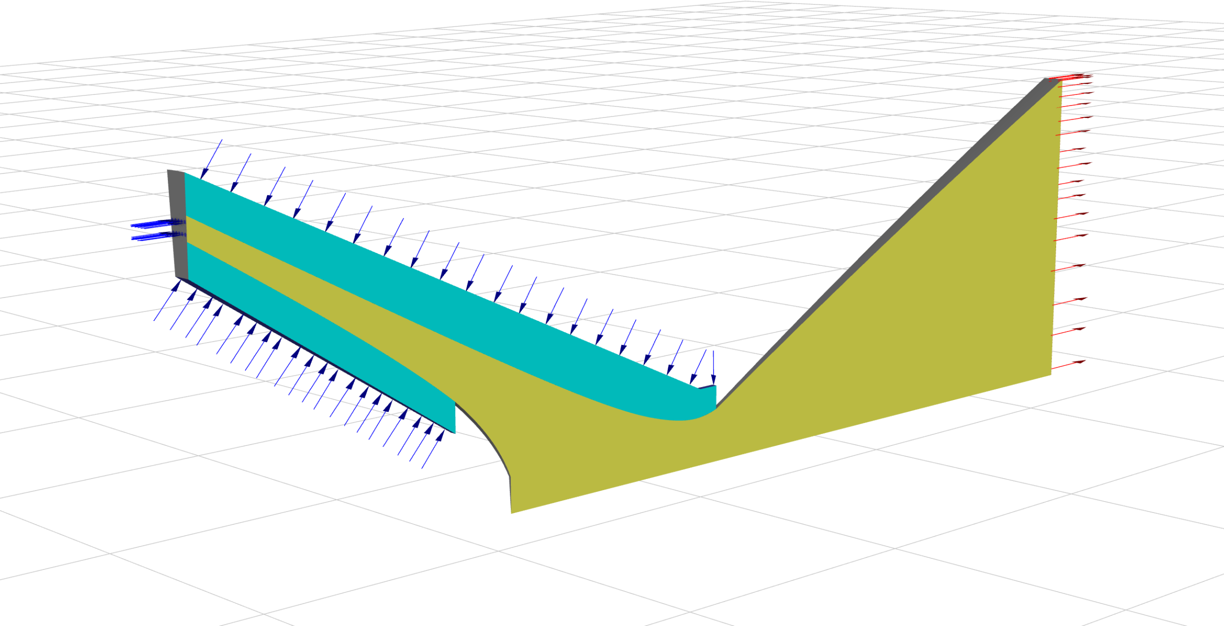

Figure 3.19: Fluent model, in which the CMC liners are modeled as a porous domain in addition to the engine interior.

3.5 Combustion model

The first step in validating the combustion model is to examine the temperature curve for temperature increases in the expected ranges. This has already been done in the previous consideration of the temperature profile, where in Figure 3.7, areas of elevated temperatures of up to 3288 K arise from the inner and outer contours. Furthermore, increasing concentrations of CO_2 can be found in these areas. Figure 3.20 shows the increase in CO_2 concentration by the change from blue to green. This provides initial evidence that the combustion model is functioning as intended.

Figure 3.20: CO_2 mass fraction in the sectional view

For the validation of the estimation of the combustion, key parameters are compared with results from NASA CEA. The combustion chamber temperature and the characteristic velocity c^* were used for this purpose. Using the given parameters for combustion chamber pressure, fuel composition and temperature, as well as the area ratios of the cross-sections, NASA CEA calculates a combustion chamber temperature of 2824.61 K and a characteristic velocity of 1606.7 m/s.

The temperatures in the engine simulation reach up to 3288 K. The characteristic velocity is calculated as:

$$c^* = \frac{p_c A_t}{\dot{m}} \tag{3.2}$$

and, with a pressure of 2147932 Pa, a nozzle throat diameter of 13.8 mm, and a mass flow rate of 0.821 kg/s, results in a velocity of 1567 m/s. Accordingly, the characteristic velocity of the engine is within a plausible range just below the value given by NASA CEA. However, the combustion chamber temperature of the engine is well above the value given by NASA CEA. Because of the significant discrepancy between the NASA CEA and numerical simulation results for combustion chamber temperatures, the combustion model cannot be definitively validated. It is suspected that the model might be overestimating combustion. Considering that the combustion in the engine is not complete (hence the streak of unburned oxygen in the engine) and that the combustion temperature seems to be far overestimated by the simulation, the characteristic velocity of the simulation must be far lower than from the CEA calculation. However, the difference is less than expected which raises concerns over whether this is just due to the temperature being overestimated by the combustion model and over whether the characteristic velocity would be actually lower if the combustion model would not overestimate the combustion.

3.6 Quality of combustion

When describing the flow pattern, it was already apparent from the temperature curve that a lower temperature range extends from the injector across the entire combustion chamber in the middle of the combustion chamber gap to the exit plane. This suggests that the oxidizer flow in the combustion chamber is not completely mixed and burned. For this purpose, the mass fraction of oxygen for the entire engine is used in Figure 3.21. The plot shows that there is a higher oxygen concentration in the area where the temperature is also relatively low. As the mixing ratio is set to be slightly rich, the remaining oxygen indicates incomplete combustion. In order to assess the extent of incomplete combustion, the material concentrations determined by Ansys Fluent at the end of the expansion nozzle are evaluated and compared with the values determined by NASA CEA. Before that, however, a note must be made about the determination of the substance concentrations between the Ansys Fluent simulations and NASA CEA.

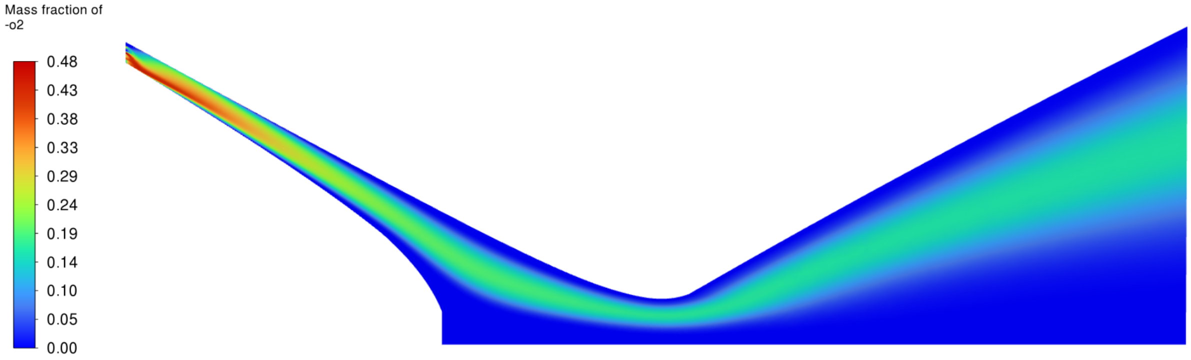

Figure 3.21: Mass fraction of O_2 along the engine.

Only water, oxygen, carbon dioxide and kerosene are modeled in the present simulations. The kerosene is modeled as just a single hydrocarbon compound ($C_{12}H_{23}$). NASA CEA models kerosene in its real form as a complex mixture of hydrocarbon chains. It also models all intermediate products that may occur in the reaction. The output at the end of the expansion nozzle is therefore numerous hydrocarbon compounds and also substances such as CO, OH, HO_2 and others. As these substances do not occur in the reactions of the Ansys Fluent simulations, they must be summarized and assigned to one of the occurring substances. The hydrocarbon compounds are combined to resemble kerosene. For the other substances mentioned, such as CO, OH and HO_2, only CO has a non-zero value. This was added to CO_2. The individual hydrocarbon compounds were present in such small numbers that their numerical values were not listed in NASA CEA results. However, since combustion is a rich process, hydrocarbon compounds must still be present at the end of the expansion nozzle even if combustion is ideal. The mass fraction of kerosene at the end of the engine in CEA is therefore determined by subtracting the mass fractions of all other substances (H_2O, O_2, CO_2 with CO) from one.

The resulting values from NASA CEA and the Ansys Fluent simulation are listed in Table 3.8. The values of Ansys Fluent are higher for the educts (oxygen and kerosene) that are consumed during combustion, while the values of Ansys Fluent are lower for the products (water and carbon dioxide) that are produced during combustion. All four substances therefore indicate that combustion is not complete. Since the combustion model assumes chemical equilibrium, incomplete combustion indicates imperfect mixing. Next, the influence of this incomplete combustion on the performance parameters of the engine is to be investigated in order to determine the extent to which the performance of the tire engine is affected.

Table 3.8: Mass fractions of the species in the exit plane that have been calculated by Ansys Fluent and NASA CEA.

Species	Species mass fractions	
	ANSYS Fluent	NASA CEA
Water	0.5784	0.60982
Oxygen	0.0852	0
Kerosene	0.0357	0.00087
Carbon dioxide	0.3008	0.38431

3.7 Performance parameters

The performance parameters of interest are the thrust and specific impulse. Both are listed in Table 3.9 for both the Ansys Fluent and NASA CEA simulation. This means that the thrust and specific impulse of the Fluent calculation are almost 10% below the theoretically possible values according to the CEA. This means that considerable losses in the efficiency and performance of the engine are to be expected. The extent to which the lack of mixing of the substances influences the loss of performance will be examined in the following section as a new injector variant that allows for improved fuel component mixing is introduced.

Table 3.9: Thrust and specific impulse of the engine calculated by Ansys Fluent and NASA CEA.

Parameter	Ansys Fluent	NASA CEA
Thrust	2264.56 N	2513.74 N
Specific Impulse	280.98 s	312.11 s

3.8 Variation of the injector pattern

Because the simulations were sometimes computationally intensive and the problem with incomplete mixing and combustion of the fuel components persisted, the idea arose to redesign the engine's injector so that:

- **its pattern repeats itself within smaller intervals** (so the computing domain is narrower and requires less cells)
- **its pattern is not periodic**, but symmetrical (for less flow induction in circumferential direction)
- **it can also inject part of the fuel mass flow into the engine** (to investigate the mixing of the components)

The existing slot openings of the injector were converted into 1 mm holes. These are to be finely distributed around the circumference of the injector. The surface area of all 1 mm holes should correspond to the surface area of the slot openings of the old injector. This results in 840 holes distributed across the entire injector. The holes were arranged in two rings, each with 420 holes. In order to be able to feed the fuel into the combustion chamber through the injector, another ring with 420 1 mm holes was added. A close up view of the new injector pattern is shown in Figure 3.22. The outer and inner rings are intended for injecting the oxidizer, while the middle ring is for injecting the fuel. It should be noted that the injector is intended for experimental research. So, while the injector openings are close together, resulting in thin walls between them, which may make it too difficult to manufacture for a real-world model, the injector pattern is viewed as sufficient for now. A section measuring 5 holes wide was then extracted from this injector. This results in a section that is 4.28° wide. This reduction of the domain in width significantly reduces

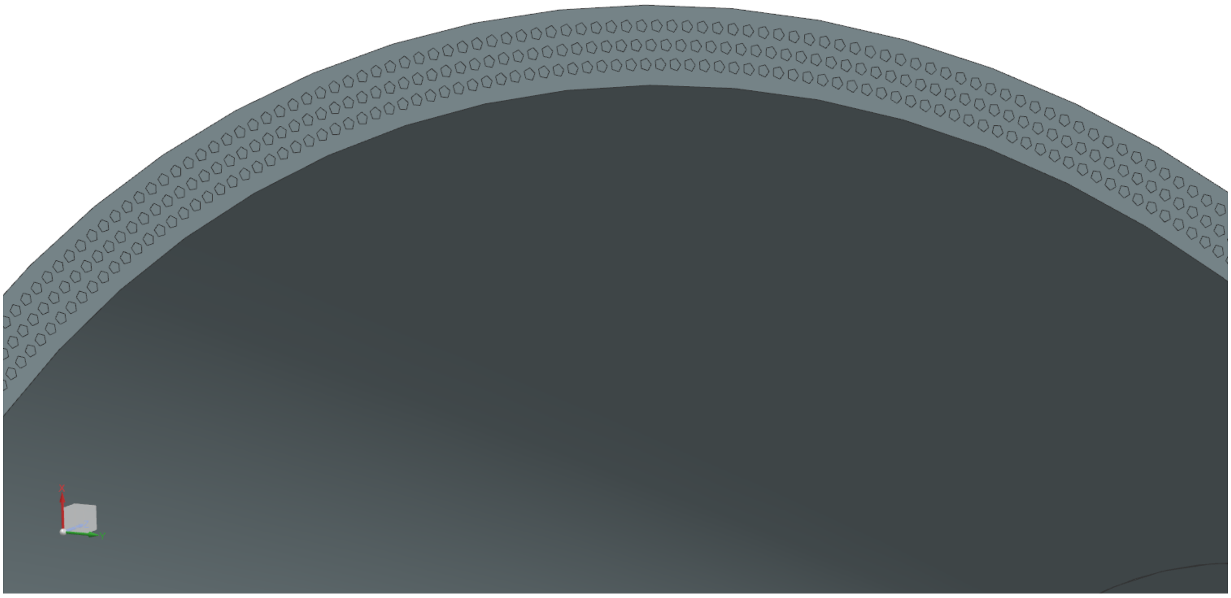

Figure 3.22: Closeup of the new experimental injector pattern

the number of cells while maintaining the same fine mesh. To obtain the standard from the mesh study, the section was meshed with the same parameters as mesh 5 (see Table 3.1). This resulted in a cell count of 211,629 elements, which corresponds to a cell density of 49,446 elements per degree. Surprisingly, this is higher than for mesh 5, which has a cell density of 34,896 elements per degree with 1,046,891 cells at 30°. Although it was expected, that both meshes would have the same cell density per degree since both have the same meshing parameters, the higher cell density promises higher resolution with lower computational effort.

In order to achieve better mixing of the components in the combustion chamber, the oxidizer was not injected in a straight line in the direction of flow, but along the generatrices of the outer hyperboloid. These have a component in the circumferential direction. The oxidizer from the outer ring of the injector was injected in a different circumferential direction than that of the inner ring. This is intended to increase the turbulence of the components and their mixing. For this, the inflow vectors of the oxidizer were constructed according to Hoffmann [1]. The fraction of the engines kerosene mass flow that is injected through the injector plate has been varied from 0% up to 100% at 10% intervals. The results of the investigations with the experimental injector geometry are presented in the following.

Flow pattern

Generating the pathlines from the injector inlets, a flow pattern is obtained in which it can be clearly seen that the oxidizer is injected into the combustion chamber along the generatrix lines and also moves along them far into the combustion chamber. Figure 3.23 shows the pathlines in two views. In this simulation the injector fuel mass flow is at 50%.

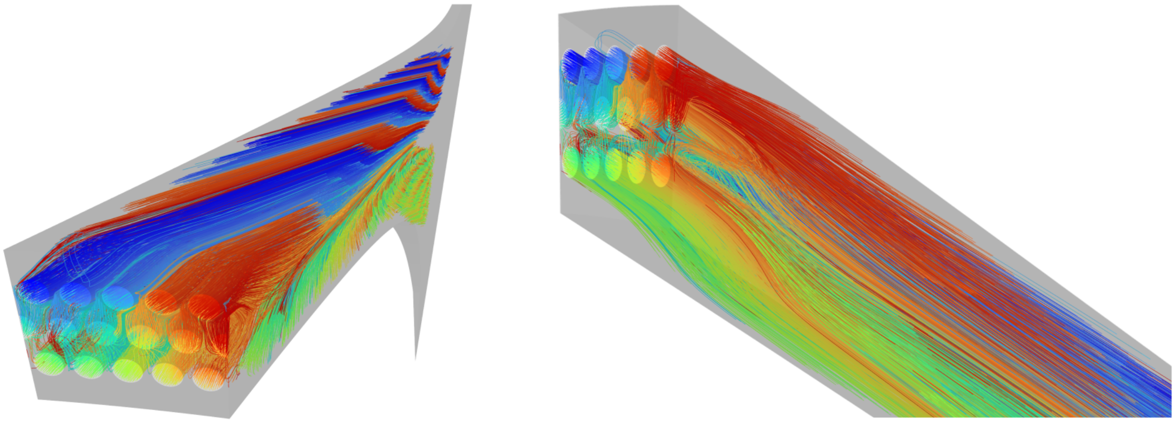

Figure 3.23: Pathlines steming from the injector openings. The amount of kerosene injected through the injector amounts to 50% of the engines kerosene mass flow

When viewed from the side, it can also be seen that the kerosene does not appear to enter the combustion chamber in large quantities and does not form a full jet. Rather, it is picked up by a vortex that transports it to the adjacent oxidizer streams, from where it is entrained. Apparently, the volume flow of kerosene is significantly lower. On the original injector in Figure 3.11, it has already been noted that particles are transported away in a circumferential direction in the immediate vicinity of the injector due to its periodic pattern. Here the paths run predominantly in the circumferential direction and sometimes move far away from the longitudinal plane, which is assumed to be associated with losses. Figure 3.24 shows that this is much less the case with the new injector.

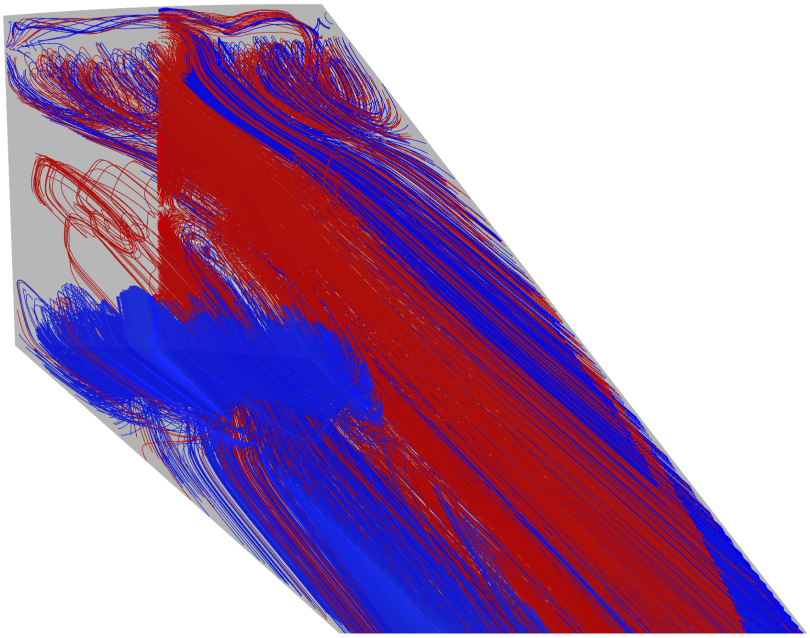

Figure 3.24: Pathlines steming from the longitudinal plane. The amount of kerosene injected through the injector amounts to 50% of the engines kerosene mass flow

The image shows the paths of particles that also originate from the longitudinal plane. It can be seen that the particles also leave the plane, but the component in the circumferential direction is significantly smaller compared to the original injector in Figure 3.11. Rather, these are deviations with the main direction of movement in the direction of the nozzle throat. Only the upper edge of the injector has a pair of pathlines that move almost exclusively in the circumferential direction. These are significantly less pronounced and lower in number than with the original injector. The conclusion is that the new injector results in fewer uncontrolled movements in the circumferential direction, which makes the injector more efficient. This underlines the hypothesis that the pronounced movements in the circumferential direction in Figure 3.11 originate from the periodic injector pattern. It is also noticeable that in the new injector variant, the flow of the oxidizer tends to adhere to the inner contour of the combustion chamber, just like with the original injector. When investigating the flow characteristics with varying injector fuel mass flows, it was found that this adhering behavior of the flow changes the more kerosene is injected through the injector. Figure 3.25 compares the vector fields of injector fuel mass flows of 0%, 50% and 100% to show this change. The picture on the left shows how the flow of the oxidizer is deflected inwards from both the opening of the inner and outer ring and attaches itself to the inner liner. A vortex forms in the free space above, which picks up kerosene on the upper side, on the contour of the outer liner, transports it to the injector and is then carried along by the oxidizer flow. In the middle picture, with 50% kerosene through the injector, it can be seen that the current coming from the inner oxidizer ring is also attaches to the contour of the inner liner. The upper oxidizer current, on the other hand, is no longer deflected towards the inner liner, it even drifts slightly towards the outer liner. The vortex that was still visible in the left picture has now disappeared. The picture on the right, at 100% of the kerosene through the injector, looks similar. An exact explanation for the changed flow pattern cannot be given at this point. It can only be said that the higher occurrence of kerosene near the injector results in a higher combustion rate. This is also accompanied by an earlier expansion of the gases due to combustion. It is possible that this context leads to less deviation of the oxidizer flows. Nevertheless, even with a higher availability of kerosene in the injector, the oxidizer flows are diverted from the injector to the liners. As already discussed for the original injector in Chap. 3.3, this means potentially failed transpiration cooling and even damage to the liners at these points. As already mentioned, future engine tests with oxide ceramics should show whether the flow phenomenon is negligible if oxidation-resistant liners are used.

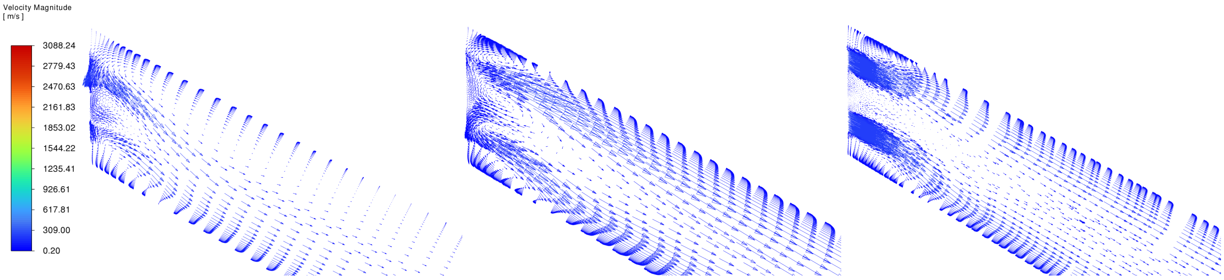

Figure 3.25: Vector field of the flow behind the injector at 0%, 50%, and 100% of kerosene through the injector

Quality of combustion

By shifting the kerosene mass flow from the liner to the injector, the combustion has changed step by step. This is reflected in the combustion chamber pressure. In Fig. 3.26, the combustion chamber pressure is plotted over the mass flow rate of the kerosene through the injector. Starting from an injector fuel mass flow of 0%, the pressure drops slightly during the step to 10%. It then increases linearly up to a proportion of 80%. At 20% it is already higher than at 0%. From 80% to 90%, the combustion chamber pressure still increases, but significantly less than in the linear segment before. From 90% to 100%, the pressure finally drops again, but it is still higher than with a kerosene injector mass flow rate of 70%. The increasing combustion chamber pressure suggests that combustion is more complete. The fact that the combustion chamber pressure initially decreases in the first step, from 10% to 20%, and also increases more slowly from 80% to 90% and finally drops to 100%, cannot be explained for the time being. The oxygen concentrations in the engine are consulted for further consideration. Of particular interest are the states at 0% injector fuel mass flow, within the linear increase, and at 90% as well as at 100%. In Figure 3.27, therefore, the mass fractions of oxygen of 0%, 50%, 90% and 100% injector fuel mass flow are shown.

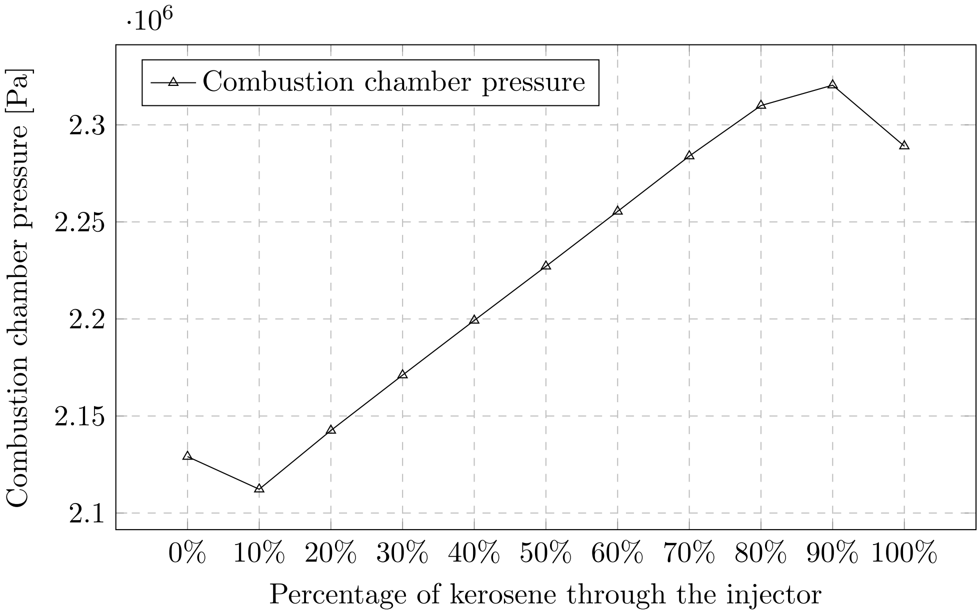

Figure 3.26: Combustion chamber pressure in dependence to the percentage of the kerosene that is injected through the injector

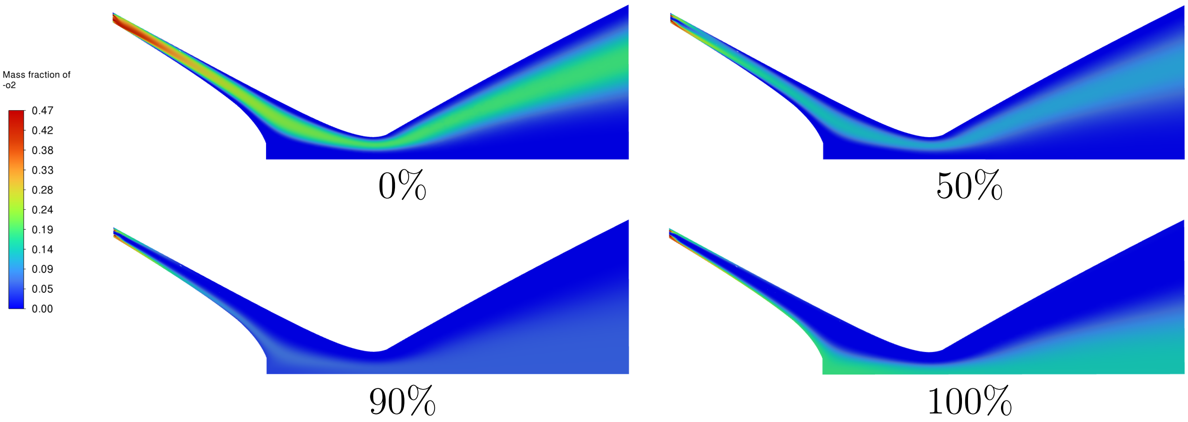

0%

50%

90%

100%

Figure 3.27: O_2 mass fraction at 0%, 50%, 90%, and 100% of the kerosene injected through the injector.

At 0% injector fuel mass flow, the oxygen concentration in the injector area is particularly high. This area takes up almost the entire height of the combustion chamber gap. In the course of the combustion chamber, areas of low oxygen concentration form starting from the outer and inner liner. This area mainly contains unburned kerosene and marks the transition to the combustion zone. However, the area of increased oxygen concentration does not disappear. It passes through the entire combustion chamber, the nozzle throat and runs through the entire expansion nozzle up to the outlet level, forming a streak that runs through the whole engine. This streak of unburned oxygen is an indication of incomplete combustion of the fuel components in the engine. The high concentration of oxygen means that combustion is still highly inefficient.

At an injector fuel mass flow rate of 50%, the streak of unburned oxygen has become significantly less pronounced, and that along the entire engine. Already at the injector, the area of increased oxygen no longer extends over the entire height of the combustion chamber gap, but is split up by an area of low oxygen concentration. Kerosene is suspected in this area, as it is injected at precisely this point on the injector. This means that at 50% injector fuel mass flow, combustion is much more complete, which can be seen from the fact that there is significantly less unburned oxygen. The more complete combustion is consistent with the higher combustion chamber pressure at 50% injector fuel mass flow. The highest combustion chamber pressure is achieved at 90% injector fuel mass flow. This is accompanied by an even lower oxygen concentration than with 50% injector fuel mass flow along the entire engine. If the injector fuel mass flow is increased to 100%, part of the oxidizer flow, and thus also the oxygen, appears to attach to the inner contour of the engine and continue through the entire engine. This again appears to be the phenomenon of the oxidizer current adhering to the inner liner, which was already noticed in the previous sections for the original injector and also for the modified injector. On closer inspection, this can be seen in all variations of the injector fuel mass flow. Only with an injector fuel mass flow of 100% does the oxygen run along the entire contour of the inner hyperboloid. In this case, the oxygen from this area seems to have difficulty mixing with the rest of the flow, which significantly reduces the completeness of combustion compared to the injector fuel mass flow of 90%. This is also consistent with the associated lower combustion chamber pressure in Figure 3.26. All in all, it can be said that combustion becomes more complete and therefore more efficient in a certain range when part of the fuel is injected through the injector. The phenomenon of the oxidizer current adhering to the inner liner continues to occur and represents an important aspect for investigation in ongoing work.

A look at the mass fractions of the components in the expansion nozzle supports the previous findings. In Figure 3.28, the proportion of the individual substances in the outlet plane of the expansion nozzle is plotted over the various injector fuel mass flows. The curves with a continuous contour represent the calculated mass fractions from Ansys Fluent. The dashed lines are the ideal values determined by NASA CEA. Since oxygen and kerosene are consumed in an ideal combustion process, their proportion tends towards zero, while water and carbon dioxide are produced and their values assume certain levels. Since the O/F ratio of the engine is set to be slightly rich, the kerosene value is not quite zero, which is difficult to see in the diagram in Figure 3.28. The diagram shows that the oxygen and kerosene go towards zero over the injector fuel mass flow, while the values of water and carbon dioxide approach the ideal value determined in CEA from below. In doing so, all four substances show the same qualitative curve as the combustion chamber pressure in Figure 3.26—for oxygen and kerosene, the curve is only mirrored vertically. From an injector fuel mass flow of 0% to 10%, the respective mass fraction first moves away from the ideal value. The mass fraction then approaches the ideal value linearly up to an injector fuel mass flow of 80%. The approach runs from 80% to 90% in a smaller step and reaches its best value. Towards 100%, the mass fractions move away from their ideal values again.

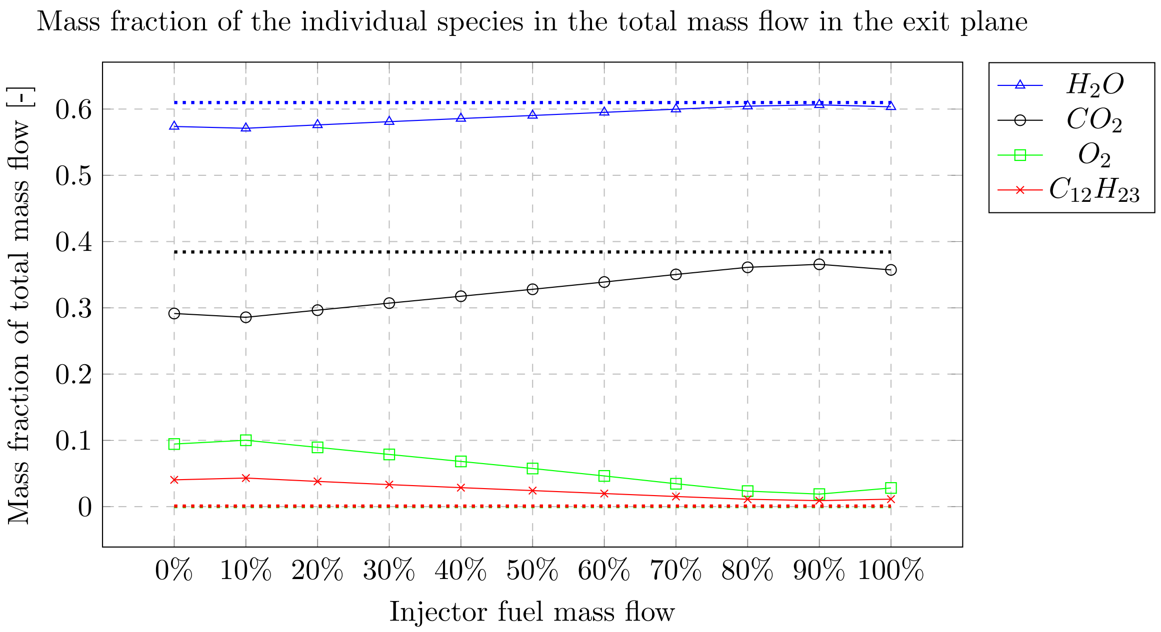

Figure 3.28: Display of the proportion of the individual species in the total mass flow in the exit plane. Dottes lines mark the ideal values that have been calculated by NASA CEA.

Accordingly, the completeness of the combustion exhibits exactly this behavior. Consequently, the combustion can be improved by allowing the modified injector to also inject kerosene into the combustion chamber through the injector. The optimum of the combustion takes place when 90% of the kerosene mass flow is injected through the injector. However, the more of the kerosene is injected through the injector, the less remains available for transpiration cooling, which is critical for the engine and for which the engine was specifically designed in the first place. In the future, therefore, a way must be found to increase the efficiency of combustion without leaving too little kerosene available for transpiration cooling. For this purpose, it will be necessary to increase the accuracy of the transpiration cooling model and to understand the flow characteristics of the engine more precisely, especially with regard to the contact of the oxidizer flows with the liner walls. However, these considerations are part of future work. In the following, the influence of the varying injector fuel mass flow on the performance data of the engine shall be examined.

Performance parameters

The performance parameters to be examined here are the thrust and the specific impulse. Both are plotted in a diagram over the injector fuel mass flow in Figure 3.29. Note that the curves of both variables coincide due to suitable scaling. As expected, the thrust and the specific impulse also show the same curve as already seen in the combustion chamber pressure and the mass fractions in Figures 3.26 and 3.27. From an injector fuel mass flow of 10% to 20%, the performance values decrease and then increase linearly up to 80%. From 80% to 90%, the ascent is flatter. Towards 100%, the values decrease again to below the level of 80% injector fuel mass flow. Several parameters now unanimously indicate the most efficient mixing and thus the most efficient combustion as well as the highest performance with an injector fuel mass flow of 90%. Hereby, a thrust of 2442.37 N or a specific impulse of 303.24 s is achieved. This thrust deviates only 2.84% from the value calculated in CEA which far lower than with the original injector, where the deviation was 10%. So, the completeness of the mixing of the fuel components does indeed influence the performance of the engine in the Ansys Fluent simulations. It should, again, be noted, of course, that in this new configuration at 90% injector fuel mass flow only 10% of the kerosene would be available for transpiration cooling. It is, therefore, important to find a way to increase the mixing in the combustion chamber and to dimension the transpiration cooling sufficiently. In Chapter 3.5, the assumption was made that the combustion model possibly overestimates the combustion parameters, as it has determined significantly higher temperatures than NASA CEA. In view of the fact that the completeness of combustion has now been increased almost to the ideal state and the performance of the engine is now so close to the ideal value, the question arises as to whether the combustion model may still be able to determine useful performance data despite overestimating the temperature, which should be investigated further in future work.

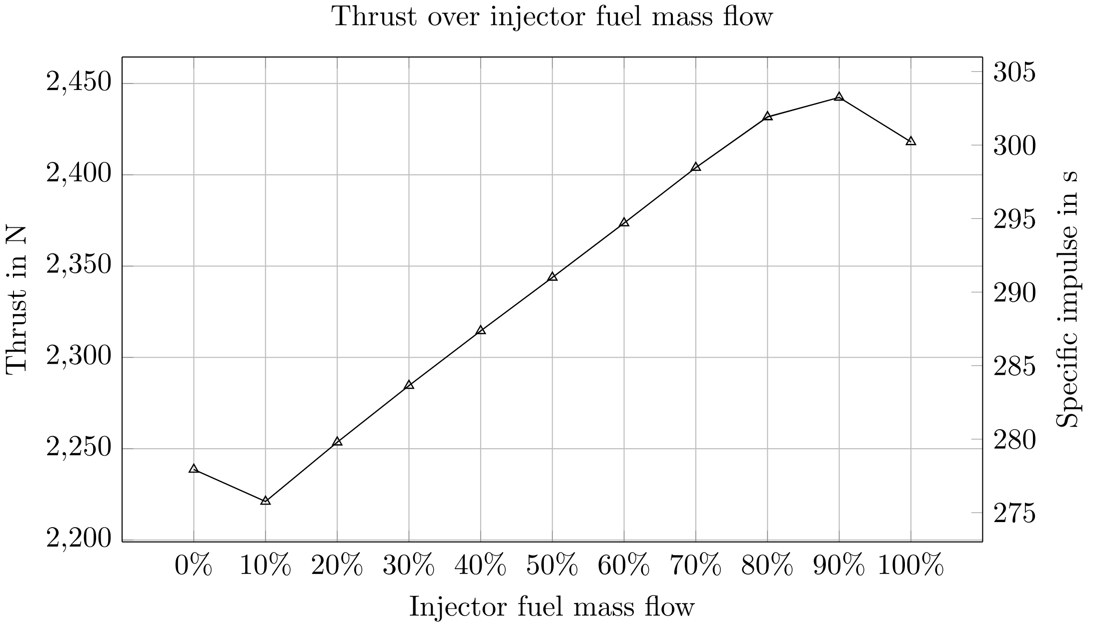

Figure 3.29: Visualization of the thrust and specific impulse over the injector fuel mass flow. Note, that both curves for the thrust and the pecific impulse are drawn in this graph but they both coinside.

3.9 Classifying the results in the context of the performance scaling

So far, the simulations reveal incomplete mixing of the fuel components with the original injector variant. The same is true for the new injector variant, but it significantly improves with more and more fuel being injected through the injector. Additionally, the chamber pressures in the simulation appear to be higher than the 20 bar derived from the NASA CEA calculation. What do the 60 kN engine simulation results and De-Risk sub-scale engine test results reveal in comparison?

The 60 kN engine reaches its highest completeness of combustion at 15-25% and its maximum thrust at 20-25% coolant mass flow. This is equivalent to 75-85% and 75-80% injector fuel mass flow, respectively. The optimum for pressure and thrust is at 75%. The simulated pressure here is 41.52 bar, compared to 40.53 bar in the NASA RPA. The thrust is 66.59 kN compared to 66.14 kN in the NASA RPA. Thus, the simulated values slightly exceed the theoretical values derived from the NASA RPA. The 2.5 kN engine is similar in some ways. It achieves optimum combustion at 90% injector fuel mass flow. This is a deviation of about 10-15% from the 60 kN engine. With a simulated pressure of 23.2 bar, it is also above the 20 bar value generated by NASA CEA, even though NASA CEA was used for this engine and not NASA RPA. However, the simulated thrust of 2,442.4 N is below the theoretical value of 2,513.73 N from the NASA CEA. The thrust curve of the 60 kN engine is bow-shaped, while the 2.5 kN engine is only bow-shaped from 100-80%, with a linear shape thereafter (it does have a bow shape from 20-0%, but the 60 kN engine has not been modeled in this regime which is why no comparison is possbile there). This difference may be due to the scaling effect, which will be described later in this section. There are similarities between the simulation results of the two engines, such as the approximate position of the optimum and higher pressures than those estimated by NASA software. However, the 60 kN engine exceeds its theoretical thrust, while the 2.5 kN engine falls short. Additionally, the thrust curve shapes differ.

The De-Risk sub-scale engine is a small engine variant (smaller than the 2.5 kN engine). It was developed to prove that it is feasible to implement the combustion of kerosene and hydrogen peroxide in a dual-shell-hyperboloid engine and to operate it for at least 30 seconds while also proving the functionality of the transpiration cooling. The targeted combustion chamber pressure is 15 bar. Figure 3.30 shows three diagrams of the 30-second test results. The first two diagrams show the temperature curves of various sensors placed in different spots inside the engine. The third diagram shows pressure curves of various sensors placed in different spots inside the engine. The sensor naming nomenclature is explained in the figure caption. Before examining the diagrams in detail, it is important to note, that due to an error during preparation, 20 seconds after the start of the test, the kerosene, which is the medium for transpiration cooling, ran out and the engine continued to run without it. In the first diagram, the orange line (T II 67 D) and the dark blue line (T IV 337 D) remain mostly constant, staying well below 400°C. The pink line (T III 292 D) remains constant below 400°C until approximately 20 seconds into the test, at which point it begins to increase exponentially until the end of the combustion process. The behavior of all three curves proves that transpiration cooling works as intended. The two remaining curves (T II 22 D and T II 45 D) increase exponentially shortly after the 20-second mark, but they also show a linear incline above the first three lines during the first 20 seconds of the test. This behavior is surprising since these two curves' sensors are in the same axial position in the engine as the sensor connected to the orange curve (T II 67 D), which delivers the lowest temperatures. This suggests that either the combustion or transpiration cooling varies along the circumferential direction, or the upper two curves are outliers, as the lower three curves indicate efficient transpiration cooling. The second diagram shows the temperature curves of sensors placed on the cold gas side (F) or inside the walls (M) of the CMC liners. All four curves exhibit stable, nearly constant behavior below 300°C until shortly after the 20-second mark, at which point the kerosene runs out. Only after that point do three of the curves show an increase in temperature. Most of the curves in the first two diagrams show constant temperatures. Only in the last ten seconds, after the transpiration cooling fuel ran out, do the recorded temperatures of these sensors start to increase. This highlights the direct correlation between temperature and transpiration cooling, indicating its effectiveness. The third diagram shows the pressure curves of multiple pressure sensors placed on the cold gas side (F), the hot gas side (D), and in between (M) of the CMC liner. With the exception of sensor (P II 0 D), the curves of all pressure sensors coincide (with a small deviations right at the start and the end of the combustion process) and show a steady, almost linear increase from just over 14 bar up to almost 17 bar over the course of the combustion window. The P II 0 D sensor curve seems to be an outlier and is disregarded in this case. The fact that the pressure increased throughout the entire test and did not stabilize suggests that the actual pressure would be even higher. The fact that the combustion chamber pressure not only reaches, but exceeds, 15 bar during the test leads to the cautious assumption that the engine experiences a high degree of oxygen burnout. However, the De-risk engine is operating with a low O/F ratio, which means there is an excess of kerosene. In Chapter 3.4, the completeness of the combustion was improved when the amount of kerosene was accidentally doubled. This suggests that the abundance of kerosene is the main cause of the high oxygen burnout. If the air-to-fuel ratio were stoichiometric, the degree of oxygen burnout would likely be lower. On the other hand, the higher combustion chamber pressure in the test compared to the dimensioning could also support the 2.5 kN engine simulations. Here the pressures calculated by the ANSYS Fluent simulations are also higher than those calculated by the NASA CEA. In this test, however, the hydrogen peroxide is emulated by injecting gaseous oxygen (GOX) and hydrogen (GH_2) in the correct ratio into the combustion chamber. Although the composition at the exit plane may be indistinguishable from the use of actual hydrogen peroxide, the combustion process is distorted by the combustion of hydrogen and oxygen in the combustion chamber, in contrast to the injection of decomposed hydrogen peroxide. Therefore, the pressures measured in the given tests might actually differ from those that would be measured if real hydrogen peroxide were used as an oxidizer.

The 2.5 kN engine has some similarities with the 60 kN engine but there is still some differences in how the thrust turns out and in the shape of the thrust curves over the injector fuel mass flow. The differences in the shape of the thrust curve might stem from the fact that the 2.5 kN engine aims to incorporate all of its transpiration cooling fluid into the combustion while the 60 kN engine due to its larger scale has less surface boundary layer volume compared to its overall combusiton chamber volume. While the conclusion of [1] is that for the 60 kN engine a dual-shell hyperboloid combustion chamber and transpiration cooling are a suitable combination, this cannot yet be definitely applied to the 2.5 kN engine. This is because the effectiveness of its transpiration cooling cannot be confirmed, as the current model cannot yet model heat flowing into the walls. The De-Risk tests show that the transpiration cooling is indeed feasible for small scale dual-shell hyperboloid engines that run on kerosene as fuel. Although the O/F ratio was particularly fuel-rich here, it can be cautiously assumed that the 2.5 kN engine will demonstrate slightly better mixing of the components and a higher degree of oxygen burnout than in the current simulations. Although the 2.5 kN will undergo extensive development, it can be concluded that the scaling is complete and successful as soon as the effectiveness of transpiration cooling is confirmed. The results from the De-Risk egnine test give a promising outlook on that. According to the scaling effect, when scaling cylindrical combustion chambers, the wall surface area increases less than proportionally to the chamber volume, causing the cooling-surface-to-volume ratio to decrease. Although larger engines require more cooling in absolute terms, this requirement is lower relative to the total mass flow. This allows for a less fuel-rich mixture ratio to be selected in larger engines. This does also apply to dual-shell hyperboloid engines. Therefore, in the context of engine scale, it is assumed that larger-scale, dual-shell, hyperboloid engines will be able to operate closer to the stoichiometric O/F ratio and overcome the difficulty of mixing the cooling flow with the free stream. [1] [16]

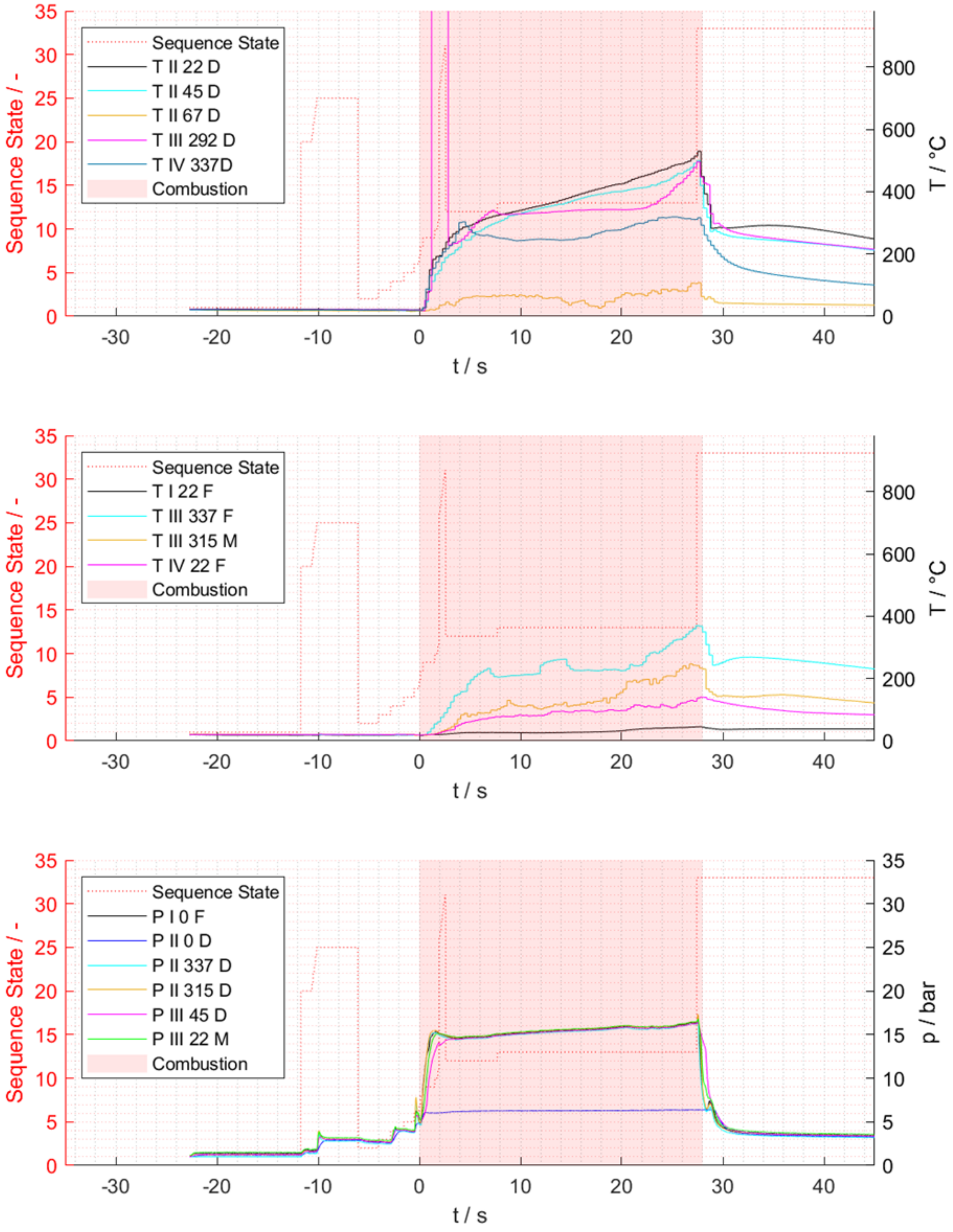

Figure 3.30: Test results of the De-Risk 30 second test run. The upper two diagrams show the temperature curves of various temperature sensors. The lower diagram shows the pressure curves of several pressure sensors. A T or P marks if the sensor is a temperature (T) or pressure sensor (P). The roman numerals mark if a sensor is placed closer to the injector (I) or to the throat (IV) in the flow direction. The arabic numerals mark at what angle in circumferential direction the sensors are placed. The letters at the end mark, if a sensor is placed on the hot gas surface of the CMC liner (D), on the cold gas side (F), or in the middle (M).

3.10 Contour of the rocket engine

In order to better validate the engine performance data with CEA, the cross-sectional areas were determined at various points in the engine model. It was found that the cross-sectional area in the combustion chamber increases in the direction of flow starting from the injector. However, this should not be the case, as it is assumed that the cross-section in combustion chambers is constant and the combustion chamber in question, with its dual-shell hyperboloid design, was deliberately designed so that the cross-sectional area remains constant. Suspecting that there might be an error in the contour design, the tool used to design the contour was checked. However, the tool appears to have been created correctly. The engine design data is also conclusive. Therefore, the data from the engine model was compared with the data from the design. Fig. 3.10 shows the contours of the design and the model superimposed on each other.

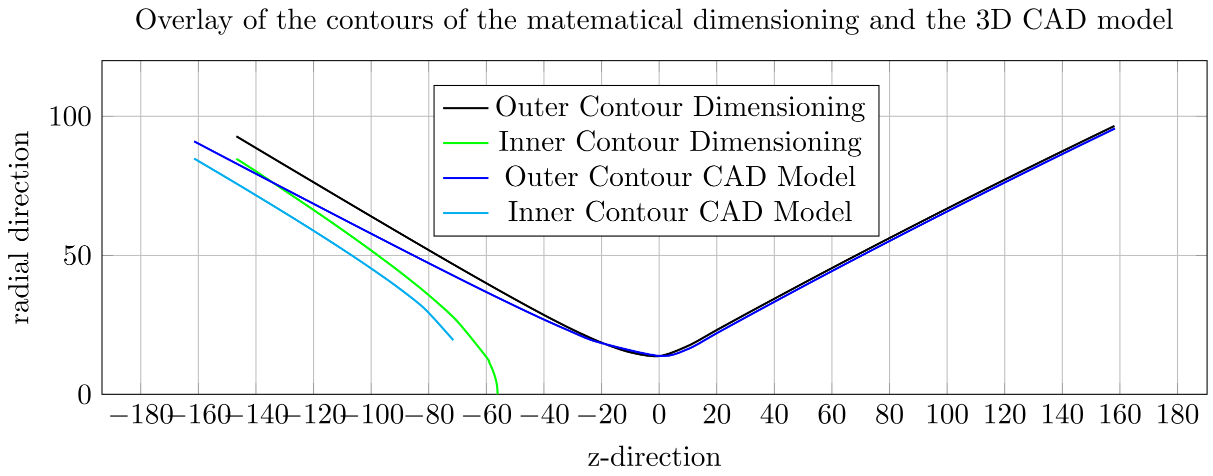
Overlay of the contours of the matematical dimensioning and the 3D CAD model

It shows that the contour of the 3D model visibly deviates from the one from the contour design tool. An error must, therefore, have occurred when transferring the contour from the design tool to the CAD program. At this point it was no longer possible to change the contour for the present thesis. For this reason, although the results of this work are suitable as a basis for understanding the flow conditions of the 2.5 kN engine, reliable results can only be obtained by first correcting the contour of the 3D model before continuing work on it.

4 Summary & Outlook

Summary

In this thesis the scaling of a 60kN dual-shell hyperboloid engine running on LOX/LCH$_4$ to a 2.5 kN engine running on HTP/Kerosene was investigated using CFD simulations in ANSYS Fluent. The first investigations show that a functioning model for the flow and combustion has been established. The correct amount of fuel was introduced into the combustion chamber through transpiration cooling. According to the vector plots, the fuel in the cooling does not enter the combustion chamber perpendicular to the surface, so that the boundary layer is blown off the surface, which suggests that the transpiration cooling may not work as intended. In addition, the results show that there is insufficient mixing in the combustion chamber. Increasing the kerosene mass flow to twice its usual value has been shown to result in much more complete combustion of the oxidizer. In this case, despite the increased cooling mass flow, the boundary layer is still not blown off the surface according to the vector field. A special occurence observed is that the flow coming from the injector adheres to the surface of the inner liner shortly after inflow, regardless of the injector geometry, which can lead to increased erosion at this point. This phenomenon is possibly caused by the geometry of the combustion chamber or the geometry in conjunction with the size of the combustion chamber. According to the setup and calculation using ANSYS Fluent, a thrust of 2.264 kN is obtained, which is in the correct order of magnitude, but still almost 10% below the design value. Despite the incomplete combustion, the simulations result in higher combustion chamber pressure and temperature, but a similar characteristic velocity than the values calculated in NASA CEA. Therefore, it is assumed that the selected combustion model misestimates combustion parameters. To investigate the completeness of the combustion, an additional injector variant was introduced, with which a portion of the fuel mass flow can be introduced into the combustion chamber via the injector. This significantly increased the completeness of combustion. A thrust of 2.442 kN was achieved, which corresponds to a deviation from the dimensioned value of 2.8%. Here, however, most of the kerosene was injected through the injector and almost no kerosene was available for the transpiration cooling. There are again deviations in pressure and temperature but a similar characteristic velocity compared to the CEA results. Thus, although the correct thrust is almost achieved with nearly complete combustion, doubts about the accuracy of the combustion model remain. The representation and simulation of kerosene proved to be much more difficult than that of hydrogen, for example, from previous work. In this work, kerosene was represented in a simplified form. The simulations carried out in this work were limited to one combustion model—no other combustion models were used for comparison. Furthermore, only one turbulence model was employed. Also, there are problems with the y^+ values, which is why the calculations need to be reviewed for fundamental errors in the modeling. In the mesh study, not the finest but a more time-efficient variant was selected—therefore, the results could be somewhat more accurate. Although the models leave room for doubt, they provide a solid foundation for initial insights, future refined models, and the ability to make relative predictions. The reults of the 60 kN engine and the 2.5 kN engine are comparable. There are deviations, for example, with regard to thrust as a function of the injector fuel mass flow, but these can be attributed to the scaling phenomenon. The scaling of the engine can be concluded as complete and successful as soon as the effectiveness of the transpiration cooling can be confirmed. The results from the De-Risk egnine test give a bright outlook on that.

Outlook

As the contour of the engine still needs to be corrected and tests are scheduled for the coming months, it is advisable to correct the engine design before production of the first version begins so that at least a correctly designed engine is available for the first test. The test data should be compared with the data from previous simulations in order to see to what extent the design deviates from reality despite the different contours. The faulty engine contour should be updated in future models and simulations. Since an updated contour entails changed flow characteristics, it is important to carry out a new mesh study before considering further simulations. As the previous simulations produced Mach numbers over 4, it is advisable to include the density-based solver in addition to the pressure-based solver in order to verify their accuracy. Then, the first thing to consider is the kerosene model. Because of its complex composition, there are several modeling approaches with different levels of complexity. In addition to the species transport model, observations can be made with another combustion model, such as the "non-premixed combustion" model. The complexity of the reaction equations can be varied. Including a multiphase model allows for modeling the kerosene's phase transition from liquid to gaseous state in the boundary layer during transpiration cooling or when flowing through the liner's walls. While these measures improve the quality of combustion modeling, multiphase modeling is computationally intensive and might exceed the scope of final theses. Nevertheless, there are approaches that can be employed to further enhance the engine's flow and combustion model. For the transpiration cooling, in addition to the implementation via the mass flow inlet and the velocity inlet, the possibility of inserting source terms for the kerosene into the cells on the surface of the liners according to [1] or to model the porous CMC liners as domains adjacent to the combustion chamber and introduce pressurized kerosene from the outside should also be investigated. The latter two variants allow the consideration of heat flows into the liner walls, which brings a considerable advantage for the evaluation of transpiration cooling. Modeling the surrounding structure of the combustion chamber and including a radiation model provides a comprehensive view of heat flow in the engine and allows for consideration of the structural design. After refining the transpiration cooling model, other turbulence models can be applied to further investigate the mixing in the combustion chamber. Once the turbulence model is more elaborate, the phenomenon of flow adhesion to the inner hyperboloid can be studied. This may require considering different combustion chamber dimensions. Furthermore, the experiment with the adapted injector geometry (Chap. 3.8) can be followed up and further experiments can be conducted to examine the mixing of gases, as well as the development of flow and combustion, depending on the injector design in order to find the most suitable configuration. The possibility of introducing kerosene into the combustion chamber through the injector should continue to be considered. In conjunction with this, the optimal O/F ratio can be investigated. Of particular interest here is how the combustion, the entire flow field, and the heat flow into the walls can be optimized by varying the local intensity of the cooling mass flow. For example, this could be done in the nozzle throat or by adjusting the ratio of the cooling mass flow through the outer liner to the cooling mass flow of the inner liner, rather than distributing it evenly based on their surface ratio.

In conclusion, it can be said that there are still many aspects and parameters of the engine that need to be investigated, and that modeling the engine is still in its early stages. The results of this work allow for initial qualitative statements about the flow, combustion, and performance of small-scale DSHTs and the use of kerosene as a fuel. These findings contribute significantly to the development of this new engine technology with the potential to overcome the disadvantages of conventional liquid rocket engines and enable more robust and efficient engines in the future. Due to the high level of pending improvements to the engine, the aspects should be worked through gradually and spread over several final theses. It remains to be said, however, that these will be very exciting.

Zusammenfassung & Ausblick

Zusammenfassung

In dieser Arbeit wurde die Skalierung eins 60 kN Dualschalen-Hyperboloid Triebwerks, welches mit LOX/LCH$_4$ betrieben wird, auf ein 2,5 kN Triebwerk, welches mit HTP/Keorsin betrieben wird, mittels CFD-Simulationen in ANSYS Fluent untersucht. Die ersten Untersuchungen zeigen, dass ein funktionierendes Modell für die Strömung und Verbrennung etabliert wurde. Dabei ist es gelungen, die richtige Menge an Brennstoff durch die Transpirationskühlung in die Brennkammer einzubringen. Der Brennstoff wird laut den Vektorplots im Kühlfilm scheinbar nicht senkrecht zur Oberfläche in die Brennkammer geblasen, sodass dort die Grenzschicht von der Oberfläche abgeblasen wird, was vermusten lässt, dass die Transpirationskühlung möglicherweise nicht wie vorgehabt funktioniert. Darüber hinaus zeigen die Ergebnisse, dass es zu keiner ausreichenden Durchmischung in der Brennkammer kommt. Bei der Verdopplung der Kerosinmenge hat sich gezeigt, dass die Verbrennung des Oxidators deutlich vollständiger verläuft. Trotz des dadurch erhöhten Kühlmassenstroms wird dabei laut Vektorfeld die Grenzschicht immer noch nicht von der Oberfläche abgeblasen. Eine besondere beobachtete Gegebenheit ist, dass die von Injektor kommende Strömung sich unabhängig von der Injektorgeometrie kurz nach Einströmen an die Oberfläche des Innenliners haftet, was dort zu einer erhöhten Erosion führen kann. Dieses Phänomen ist möglicherweise durch die Geometrie oder die Geometrie in Verbindung mit der Größe der Brennkammer bedingt. Nach dem Setup und den Rechnungen mit ANSYS Fluent erhält man einen Schub von 2,264 kN, was in der richtigen Größenordnung, jedoch noch knapp 10% unterhalb des Auslegungswertes liegt. Da die Simulationen, trotz der unvollständigen Verbrennung, gleichzeitig einen höheren Brennkammerdruck, eine deutlich höhere Brennkammertemperatur, aber eine ähnlich hohe charakteristische Geschwindigkeit als die in CEA ausgerechneten Werte ergeben, wird davon ausgegangen, dass das ausgewählte Verbrennungsmodell die Verbrennungsparameter möglicherweise verschätzt. Zur Untersuchung der Vollständigkeit der Verbrennung wurde eine weitere Injektorvariante eingeführt, mit der ein Teil des Brennstoffmassenstroms über den Injektor in die Brennkammer eingebracht werden kann. Dadurch konnte die Vollständigkeit der Verbrennung erheblich erhöht werden. Dabei wurde ein Schub von 2,442 kN erreicht, was einer Abweichung vom Auslegungswert von 2,8% entspricht. Hier kommt es allerding erneut zu Abweichungen von Druck und Temperatur bei passender charakteristischen Geschwindigkeit. Obwohl man bei einer fast vollständigen Verbrennung beinahe den richtigen Schub erhält, bleiben die zweifel an der Akkuratheit des Verbrennungsmodells weiterhin bestehen. Die Darstellung und Simulation des Kerosins hat sich als deutlich schwieriger erwiesen, als die von bspw. Wasserstoff aus vorheriger Arbeit. Das Kersoin wurde in dieser Arbeit vereinfacht dargestellt. Die in dieser Arbeit durchgeführten Simulationen waren auf ein Verbrennungsmodell beschränkt—es wurden keine Verbrennungsmodelle zum Vergleich gegengerechnet. Des Weiteren wurde nur ein Turbulenzmodell verwendet. Weiter gibt es Probleme mit den y^+-Werten, weshalb die Berechnungen auf grundlegende Fehler in der Modellierung überprüft werden müssen. In der Netzstudie wurde nicht die feinste, sondern eine zeiteffizientere Variante gewählt—die Ergebnisse könnten daher noch etwas genauer sein. Auch wenn die Modelle einzelne Zweifel offenlassen, liefern sie erste Erkenntnisse und erlauben es, relative Aussagen zu treffen. Zudem bieten sie eine solide Basis für weiterführende und ausgefeiltere Simulationen. Die Ergebnisse des 60-kN-Triebwerks und des 2,5-kN-Triebwerks lassen sich gut vergleichen. Es gibt Abweichungen, beispielsweise hinsichtlich des Schubs als Funktion des Injektorbrennstoffmassenstroms, diese lassen sich möglicherweise auf das Skalierungsphänomen zurückführen. Die Skalierung des Triebwerks kann als abgeschlossen und erfolgreich betrachtet werden, sobald die Wirksamkeit der Transpirationskühlung bestätigt werden kann. Die Ergebnisse des De-Risk-Triebwerktests lassen diesbezüglich einen positiven Ausblick zu.

Ausblick

Da die Kontur des Triebwerks noch korrigiert werden muss und in den nächsten Monaten Tests für das Triebwerk anstehen, ist angeraten, das Triebwerksdesign noch vor Beginn der Fertigung der ersten Ausführung zu korrigieren, damit zumindest für den ersten Test ein korrekt ausgelegtes Triebwerk zur Verfügung steht. Die Daten der Tests sollten mit denen der bisherigen Simulationen verglichen werden, um zu sehen, inwiefern man trotz abweichender Kontur von der Realität abweicht. In zukünftigen Simulationen soll die korrigierte Triebwerkskontur angewendet werden. Da eine veränderte Kontur veränderte Strömungseigenschaften mit sich bringt, ist es wichtig, nach dem Korrigieren der Kontur eine erneute Netzstudie durchzuführen, bevor weitere Simulationen in Betracht gezogen werden. Da bei den bisherigen Simulationen Machzahlen von über 4 entstanden sind, ist es ratsam, neben dem druckbasierten auch den dichtebasierten Solver einzubeziehen, um die Genauigkeit der Solver gegenzuprüfen. Zunächst lässt sich das Kerosinmodell betrachten. Aufgrund seiner komplexen Zusammensetzung gibt es mehrere Ansätze zu seiner Modellierung, die sich in ihrer Komplexität unterscheiden. Angeknüpft daran lassen sich neben dem Species-Transport-Modell Beobachtungen mit einem anderen Verbrennungsmodell, dem „non-premixed combustion“-Modell, durchführen. Dabei kann die Komplexität der Reaktionsgleichungen variiert werden. Durch Einbeziehung eines Multiphasenmodells kann der Phasenübergang von Kerosin vom flüssigen in den gasförmigen Zustand in der Grenzschicht der Transpirationskühlung oder beim Durchströmen der Linerwände modelliert werden. Diese Maßnahmen verbessern die Qualität der Modellierung der Verbrennung, jedoch sind Multiphasenmodellierungen rechenintensiv und könnte den Rahmen von Abschlussarbeiten sprengen. Es gibt jedoch weitere Ansätze, mit welchen man zusätzlich die Strömungseigenschaften des Triebwerks verbessert. Für die Transpirationskühlung sollte neben der Implementierung über das Massenstrom-Inlet und dem Geschwindigkeits-Inlet auch die Möglichkeiten untersucht werden, Quellterme für das Kerosin gemäß [1] in die Zellen auf der Oberfläche der Liner einzufügen oder das Implementieren der porösen Liner als Domains, welche an die Brennkammer angrenzen und von außen mit Kerosin als Druckrandbedingung beaufschlagt werden, untersucht werden. Die beiden letztgenannten Varianten ermöglichen die Betrachtung von Wärmeströmen in die Linerwände, was einen erheblichen Vorteil für die Bewertung der Transpirationskühlung mit sich bringt. Die Modellierung der umgebenden Struktur der Brennkammer und das Einbeziehen eines Strahlungsmodells ermöglicht eine ganzehitliche Betrachtung der Wärmeströme im Triebwerk und eröffnet die Betrachtung der strukturellen Auslegung. Nach der Verfeinerung der Modellierung der Transpirationskühlung, kann die Durchmischung in der Brennkammer weiter untersucht werden, indem weitere Turbulenzmodelle in der in den Simulationen verwendet werden. Sobald das Turbulenzmodell weiter ausgearbeitet ist, lässt sich das Phänomen der am Innenhyperboloid anliegenden Strömung untersuchen. Hierfür sind eventuell Betrachtungen mit variierenden Brennkammerdimensionierungen notwendig. Darüber hinaus lässt sich an das Experiment mit der angepassten Injektorgeometrie (Kap.3.8) anknüpfen und weitere Experimente zur Vermischung der Gase und zur Entwicklung der Strömung und Verbrennung in Abhängigkeit vom Injektor durchführen, um die geeignetste Konfiguration zu ermitteln. Dabei soll weiterhin in Betracht gezogen werden, das Kerosin auch durch den Injektor in die Brennkammer einzubringen. In diesem Zusammenhang kann auch das optimale O/F-Verhältnis untersucht werden. Hier könnte es besonders interessant sein, zu untersuchen, wie sich die Verbrennung und das gesamte Strömungsfeld sowie der Wärmestrom in die Wände optimieren lassen, wenn man die örtliche Intensität des Kühlmassenstroms variiert, beispielsweise im Düsenhals, oder das Verhältnis des Kühlmassenstroms durch den äußeren Liner zum Kühlmassenstrom des inneren Liners verändert und nicht nur an deren Oberflächenverhältnis festmacht.

Abschließend lässt sich sagen, dass es noch zahlreiche Aspekte und Parameter des Triebwerks zu untersuchen gilt und dessen Modellierung sich noch in den Anfängen befindet. Die Ergebnisse dieser Arbeit ermöglichen erste qualitative Aussagen über kleinbauende DSHT und die Verwendung von Kerosin als Brennstoff und bieten eine Grundlage für zukünftige Arbeiten, in denen die Simulationen weiter ausgebaut und verfeinert werden. Sie tragen maßgeblich zur Entwicklung einer neuen Triebwerkstechnologie bei, welche das Potenzial hat, die Nachteile herkömmlicher Flüssigraketentriebwerke zu überwinden und robustere und effizientere Triebwerke in der Zukunft zu ermöglichen. Aufgrund des hohen Ausmaßes der noch ausstehenden Verbesserungen des Triebwerks sollten die Aspekte nach und nach abgearbeitet und auf mehrere Abschlussarbeiten verteilt werden. Es bleibt aber zu sagen, dass diese Arbeiten sehr spannend sein werden.

Bibliography

[1] Hoffmann, M.: “Abschätzendes, skalierendes CFD-Screening eines neuartigen Dual-Schalen Hyperboloid-Designs in der 60 kN Schubklasse eines LOX/LCH4-Antriebs”. Studienarbeit. Technische Unversität Kaiserslautern, 2021.

[2] Ortelt, M.; Hald, H.: “Structural Investigations on Cryogenically Operated and Transpiration Cooled Fiber Reinforced Rocket Thrust Chambers”. In: *Proceedings of the 5th European Conference for Aeronautics and Space Sciences (EUCASS)*. Munich, Germany, July 2013. URL: `https://elib.dlr.de/83457/`.

[3] Ortelt, M. Hald, H.; Müller, I.: “Status and Future Perspectives of the CMC Rocket Thrust Chamber Development at DLR”. In: *Proceedings of the 65th International Astronautical Congress (IAC 2014)*. Paper ID: IAC-14,C4,3,2. Toronto, Canada: International Astronautical Federation (IAF), Sept. 2014. URL: `https://elib.dlr.de/93193/`.

[4] Ortelt, M. et al.: “Advancement of Rocket Engine Performance Through Novel Approaches for Thrust Chamber Design”. In: *Proceedings of the 68th International Astronautical Congress (IAC 2017)*. Paper ID: IAC-17,C4,10,11,x39688. Adelaide, Australia: International Astronautical Federation (IAF), Sept. 2017. URL: `https://elib.dlr.de/116522/`.

[5] Munk, D. et al.: “Analysis of a transpiration cooled LOX/CH4 rocket thrust chamber”. In: *International Journal of Heat and Mass Transfer* 182 (Jan. 2022), p. 121986. DOI: `10.1016/j.ijheatmasstransfer.2021.121986`. URL: `https://doi.org/10.1016/j.ijheatmasstransfer.2021.121986`.

[6] Messerschmid, E.; Fasoulas, S.: *Raumfahrtsysteme - Eine Einführung mit Übungen und Lösungen*. 5th ed. Berlin, Heidelberg: Springer Vieweg, 2017. ISBN: 978-3-662-49638-1. DOI: `10.1007/978-3-662-49638-1`.

[7] Schweikert, S.: “Ein Beitrag zur Beschreibung der Transpirationskühlung an keramischen Verbundwerkstoffen”. PhD thesis. Dec. 2019. DOI: `10.18419/opus-10668`.

[8] Gordon, S.; McBride, B. J.: “Computer Program for Calculation of Complex Chemical Equilibrium Compositions and Applications”. In: *NASA Reference Publication 1311* (1996).

[9] ANSYS, Inc.: *ANSYS Fluent Theory Guide*. 2024 R2. Dokumentation der Software ANSYS Fluent. ANSYS, Inc. Canonsburg, PA, USA, 2024. URL: `https://www.ansys.com`.

[10] Zeng, W. et al.: “Chemical kinetic simulation of kerosene combustion in an individual flame tube”. In: *Journal of Advanced Research* 5.3 (2014), pp. 357–366. ISSN: 2090-1232. DOI: `https://doi.org/10.1016/j.jare.2013.06.002`. URL: `https://www.sciencedirect.com/science/article/pii/S2090123213000817`.

[11] Singh, A.; Mukhopadhyay, S.: “Comparison of pressure-based and density-based solvers for scramjet modeling”. In: *AIP Conference Proceedings* 2584.1 (May 2023), p. 030007. ISSN: 0094-243X. DOI: `10.1063/5.0128250`. eprint: `https://pubs.aip.org/aip/acp/article-pdf/doi/10.1063/5.0128250/17358012/030007_1_5.0128250.pdf`. URL: `https://doi.org/10.1063/5.0128250`.

[12] Ou, G.-H. et al.: “A fully coupled Pressure-Based method for compressible flows at all Mach numbers”. In: *Applied Thermal Engineering* 255 (2024), p. 123916. ISSN: 1359-4311. DOI: `https://doi.org/10.1016/j.applthermaleng.2024.123916`. URL: `https://www.sciencedirect.com/science/article/pii/S1359431124015849`.

[13] *What are pressure-based solver vs. density-based solver in FLUENT? — Ansys Knowledge.* [Online]. Ansys. 2023. URL: `https://innovationspace.ansys.com/knowledge/forums/topic/what-are-pressure-based-solver-vs-density-based-solver-in-fluent/` (visited on 09/06/2025). Abgerufen am: 06.09.2025.

[14] Sutton, G. P.; Biblarz, O.: *Rocket Propulsion Elements.* Ninth. John Wiley & Sons, 2017. ISBN: 978-1118182748.

[15] Innocentini, M. D. M. Pardo, A. R. F.; Pandolfelli, V. C.: “Influence of Air Compressibility on the Permeability Evaluation of Refractory Castables”. In: *Journal of the American Ceramic Society* 83.6 (2000), pp. 1536–1538. DOI: `https://doi.org/10.1111/j.1151-2916.2000.tb01426.x`. eprint: `https://ceramics.onlinelibrary.wiley.com/doi/pdf/10.1111/j.1151-2916.2000.tb01426.x`. URL: `https://ceramics.onlinelibrary.wiley.com/doi/abs/10.1111/j.1151-2916.2000.tb01426.x`.

[16] Ortelt, M.; Schimpf, A.: *KEROPEX De-Risk - Final Report.* Black Engine Aerospace GmbH, Heilbronn, Germany, 2024.